NTNU

Norwegian University of
Science and Technology

Condition Monitoring of an Electro-Mechanical Shear Ram Actuator

Dagfinn Nærheim

Master of Science in Industrial Cybernetics
Submission date: June 2018
Supervisor: Tor Engebret Onshus, ITK

Norwegian University of Science and Technology
Department of Engineering Cybernetics

Problem Description

Electrical Subsea & Drilling has designed a concept for an electrically operated subsea blowout preventer (BOP), a technology that is expected to improve safety, efficiency and functionality of BOP systems. An all-electric control system will enable access to system condition at a higher level than what is possible with hydraulic systems, and increase the opportunities for condition monitoring.

The main interest of this master's thesis project is to study the condition monitoring capabilities of an electro-mechanical shear ram actuator. The shear ram actuator is part of the all-electric subsea BOP control system design, and is used to activate the shear ram barrier during a well control event. Several potential actuator faults and their detectability will be studied through modeling and simulations.

The following subtasks are proposed for the project,

- Develop a mathematical model of the electro-mechanical shear ram actuator, including motor, motor controller, mechanical transmission, and the barrier element
- Map and model potential actuator faults
- Simulate the shear ram actuator model with and without faults
- Analyze the results obtained from the simulations with regards to fault detection

Abstract

The changeover from electro-hydraulic to all-electric control systems in blowout preventers (BOP) are expected to improve the abilities of condition monitoring and early detection of system faults. This is an interesting topic on both authority and user level, and can be used to improve system reliability and decision support systems for condition-based maintenance.

Electrical Subsea & Drilling has developed an all-electric BOP control system design. The design includes an electro-mechanical shear ram actuator that serves as the driving force for the shear ram block, which is a closing element designed to cut the drill pipe and seal the wellbore, and is normally used as a last resort if well control can not be restored. The actuator consists of electric motors and mechanical transmissions, and has been studied in order to investigate its condition monitoring capabilities.

A mathematical model of the shear ram actuator has been developed in Matlab/Simulink by use of the Simscape environment. In total four mechanical faults are implemented in the model, and investigated through analysis of data obtained from simulations of the model. The faults studied regarded planetary gear tooth cracks and wear, bearing damage and increased shear ram friction. The results of this study indicate a potential for detection of all faults considered, by analysis of system parameters such as stator currents and vibrations in the torsional and translational response of mechanical components.

Sammendrag

Overgangen fra elektro-hydraulisk til et helelektrisk kontrollsystem i utblåsningssikringer (eng. *blowout preventer*, fork. *BOP*) forventes å øke mulighetene for tilstandsovervåkning og tidlig deteksjon av systemfeil. Dette er et interessant tema både på myndighets- og brukernivå, og kan potensielt sett bidra til å forbedre systemets pålitelighet. Samtidig kan overvåkningsdata brukes til å understøtte beslutninger for tilstandsbasert vedlikehold, og dermed føre til kostnadsbesparelser og økt effektivitet.

Electrical Subsea & Drilling har utviklet et elektrisk BOP-design. Designet inkluderer en elektro-mekanisk aktuator som fungerer som drivkraften til en kutteventil, som er et element utformet for å kutte over borestrengen og tette igjen brønnhullet i en nødsituasjon. Aktuering av kutteventilen er normalt sett siste utvei dersom det ikke er mulig å gjenopprette kontroll over en brønn ved hjelp av andre metoder. Aktuatoren består av elektriske motorer og mekaniske transmisjonselementer, og har blitt studert for å undersøke mulighetene for tilstandsovervåkning.

En matematisk modell av aktuatoren har blitt utviklet i Matlab/Simulink ved bruk av Simscape. Totalt fire mekaniske feil har blitt implementert i modellen, og analysert ved hjelp av simuleringsdata. Feilene som har blitt studert inkluderer tannsprekker og slitasje på planetgir, skade på motorlager og økt ventil-friksjon. Resultatene viser at alle feilene som har blitt studert potensielt sett kan detekteres ved hjelp av analyse av systemparametere som statorstrøm og torsjonale og translasjonelle vibrasjoner i ulike mekaniske komponenter.

Conclusion

This thesis investigates how specific faults in an electro-mechanical shear ram actuator can be detected by analysis of system parameters obtained through modeling and simulation of the system. A mathematical model of the actuator was derived, in which four different actuator faults were implemented. Simulations were executed to determine how the faults affected the system, and which parameters may be used for fault detection.

The first fault regarded a planetary gear tooth crack, implemented at the sun gear of each of the two planetary gears in the transmission. The fault was implemented at one gear at a time, while the opposing gear was assumed healthy. No specific frequencies in the stator current spectra related to the fault were detected. However, the tooth cracks appeared as torsional vibrations in the torsional response of the gear output shafts. A purely torsional model was used in this study, neglecting translational effects in the system. The torsional vibrations were assumed to affect the translational vibration response of the bearings supporting the output shafts of the planetary gears. Based on these results and assumptions, both the output shaft rotary encoder and bearing accelerometers are expected to provide fault detection abilities of planetary gear tooth cracks.

The second fault regarded planetary gear wear, implemented as an overall reduction in the gear mesh stiffness. The results showed that the torsional vibrations increased with the amount of wear. As with the tooth cracks, the output shaft rotary encoder and bearing accelerometers were expected to provide fault detection abilities. Further, it was observed that the torsional vibrations were reflected onto the stator current, which was subject to oscillations at the mesh frequencies of the gears. A local increase of the gear mesh frequency magnitudes in the stator current spectrum could be used as a general fault indicator for the planetary gears, as this was a result of both tooth cracks and an increase of wear.

The third fault regarded a motor bearing fault, where an outer race damage was implemented. The fault appeared in the stator current spectrum as a clear peak at the expected fault frequency. Two damage widths were studied, with almost identical results.

The results confirm that stator current analysis may be used for bearing fault detection.

The fourth fault regarded increased shear ram block friction, which was introduced by gradually increasing the friction coefficients of the friction model. Small increments of the motor current RMS were observed as the friction increased. However, as the friction force was significantly smaller than the opposing force related to the wellbore pressure, it is uncertain if current monitoring is a reliable technique for detection of increased friction. Regardless, it is clear that a well-developed monitoring system that accounts for varying external pressures is required for detection of such faults.

Preface

This thesis concludes a Master of Science degree in Industrial Cybernetics from the Department of Engineering Cybernetics at the Norwegian University of Science and Technology. The thesis builds on a pre-project carried out in the fall semester of 2017.

The study was performed in collaboration with Electrical Subsea & Drilling, who has provided technical specifications of an electrical blowout preventer system. The idea to the project was brought up together with co-supervisor Magne Rød in Electrical Subsea & Drilling.

I would like to thank my supervisor Prof. Tor E. Onshus for the feedback I have received during the work with this project. I would also like to thank Magne Rød and Egil Eriksen from Electrical Subsea & Drilling for valuable input regarding the electrical blowout preventer system's functionality and construction. Finally, I would like to thank Amir R. Nejad for his guidance regarding modeling of planetary gear sets.

Dagfinn Nærheim
Trondheim, June 2018

Contents

List of Figures

List of Tables

Abbreviations

BMS Battery Monitoring System.

BOP Blowout Preventer.

BSEE The Bureau of Safety and Environmental Enforcement.

CBM Condition-Based Maintenance.

CF Crest Factor.

E/H MUX Electro-Hydraulic Multiplex Control System.

ESD Electrical Subsea & Drilling.

FFT Fast Fourier Transform.

IGBT Insulated-Gate Bipolar Transistor.

LMRP Lower Marine Riser Package.

MCSA Motor Current Signature Analysis.

MMF Magnetomotive Force.

MT Metric Tons.

NPT Non-Productive Time.

OCS U.S. Outer Continental Shelf.

PH Pilot Hydraulic Control System.

PI Proportional-Integral Controller.

PMSM Permanent Magnet Synchronous Motor.

PWM Pulse Width Modulation.

RMS Root Mean Square.

RTM Real-Time Monitoring.

WCR Well Control Rule.

Nomenclature

C_{rp_i} ring-planet mesh damping.

C_{sp_i} sun-planet mesh damping.

F_a force applied from the shear ram actuator on the shear ram block.

F_c Coulumb friction force.

F_f force applied on the shear ram block due to friction.

F_p force applied on the shear ram block due to wellbore pressure.

F_s Stiction force.

F_n lead screw axial output force.

J_c carrier moment of inertia.

J_m motor inertia.

J_s sun gear moment of inertia.

J_p planet gear moment of inertia.

K_{rp_i} time-varying ring-planet mesh stiffness.

K_{sp_i} time-varying sun-planet mesh stiffness.

L_{sc} screw thread lead.

N_p number of planet gears.

N_s number of sun gear teeth.

N number of permanent magnet pole pairs.

R_{sg} spur gear ratio.

T_e electromagnetic torque.

T_m mechanical torque of the motor.

$T_{sg,in}$ spur gear input torque.

$T_{sg,out}$ spur gear output torque.

Θ_{p_i} angular distance between planets with respect to the first planet p_1.

λ_m rotor permanent magnet flux.

μ_c Coulumb friction coefficient.

μ_s Stiction coefficient.

ω_r rotor angular velocity.

ω_s sun gear angular velocity.

ω_r^* rotor reference angular velocity.

$\omega_{sg,in}$ spur gear input angular velocity.

$\omega_{sg,out}$ spur gear output angular velocity.

θ_c carrier angular displacement.

θ_e rotor electrical angle.

θ_r rotor mechanical angle.

θ_s sun gear angular displacement.

θ_{p_i} planet gear angular displacement.

d_f bearing damage width.

f_e electrical supply frequency.

f_m gear mesh frequency.

$f_{f,bf}$ bearing fault frequency.

$f_{f,pg}$ planetary gear fault frequency.

f_{outer} outer race fault frequency.

f_{sw} PWM switching frequency.

g gravity.

i_d d-axis stator current.

i_q q-axis stator current.

k_{loss} mesh stiffness loss due to tooth crack.

k_{max} maximum gear mesh stiffness.

k_{min} minimum gear mesh stiffness.

m_r shear ram block mass.

r_{bc} carrier base radius.

r_{bp} planet gear base radius.

r_{bs} sun gear base radius.

v_r shear ram block velocity.

v_s characteristic Stribeck friction velocity.

v_n lead screw nut translational velocity.

Chapter 1

Introduction

This introductory chapter will give a motivation for the problem to be solved, an outline of the report and an introduction to the software used.

1.1 Motivation

Today's electro-hydraulic blowout preventer (BOP) control system technology is in principle the same as it has been for many decades. The most important development over the years is that the BOP equipment has been adapted for greater depths, higher pressures, and higher cutting requirements with components of recent date. However, these adaptions have their price, and as a result, the weight of a BOP stack has more than doubled since the 1980's.

A study conducted by MCS Kenny found that control system failures are the leading cause of BOP failures [1]. One of the potential causes for the non-productive time (NPT) of drilling equipment may be the fact that current BOP systems are based on hydraulics technology, which has problems with leakages, contaminated hydraulic fluids, seal failures, shuttle-valve failures, etc.

Electrical Subsea & Drilling (ESD) has developed a new design concept for an electrically operated blowout preventer system with advanced barrier elements that will over-

come the limitations of legacy systems, surpass new regulatory requirements and provide;

- Improved safety
- Reduced NPT
- Reduced BOP stack size and weight
- Improved condition monitoring and condition-based maintenance (CBM)
- Elimination of hydraulic control fluids and discharge to environment

Declining oil prices have made it necessary for oil and gas companies to scrutinize their operations and associated costs. This has led to new interest in digitalization initiatives in the oil and gas industry. The all-electric BOP controls approach fits well into this market trend, as electrical components are inherently easier to monitor than their hydraulic counterparts. Improved system and component monitoring and tracking of operation cycles will provide valuable information regarding the operational status of the equipment. The well barrier's exact position and applied forces of an operation will be known, removing uncertainty whether a cutting operation was successful or not. Knowing the condition of a subsea BOP and control system will support evaluations for "well jumping" on larger subsea development fields.

Improved condition monitoring can be used as input for maintenance operations or replacement of components, before they turn into major failures, which could potentially lead to catastrophic results during operation. This includes monitoring of actuators, control system, electrical distribution and battery bank. Condition monitoring can potentially reduce time consumed for in-between well maintenance and remove unnecessary periodic maintenance based on known conditions of BOP components. This "known" condition can be established based on equipment performance and history, as well as real-time monitoring of the equipment by signature testing and verification through instrumentation.

New maintenance models are emerging as a response to the call for better uptime and reduced expenditure. Continuous maintenance work to reduce the required work scope and time spent during the 5-year Special Periodical Survey (SPS) yard stay is one such

approach, which will be supported by condition monitoring and condition-based maintenance.

1.2 Outline

This thesis investigates how specific faults in the electro-mechanical shear ram actuator can be detected by analysis of system parameters, including the stator current, acquired through modeling and simulation of the system. The research concerns an investigation of related work regarding modeling and fault detection. A complete model of the electro-mechanical shear ram actuator is presented, and several potential actuator faults are introduced and implemented in the model. The model is simulated with and without faults. Analysis of the simulations is carried out to determine whether the specific fault is detectable by the available system parameters.

Chapter 2 includes an introduction to condition monitoring and CBM, as well as signal processing techniques. Chapter 3 covers background theory regarding BOP systems, and the construction and functionality of the electrical BOP system. Chapter 4 covers the design of the electro-mechanical shear ram actuator, in addition to potential faults. Chapter 5 addresses the modeling of the electro-mechanical shear ram actuator and how the various faults are implemented in the model. Chapter 6 concerns the techniques used for fault detection of the respective actuator faults. Chapter 7 presents the results of the simulations and analysis, while Chapter 8 provides a discussion of the methods used, results, and further work.

1.3 Software

Matlab R2018a is used for modeling, simulation and signal processing. The model components are created in the Matlab based Simscape language and simulated in the Simulink environment.

Chapter 2

Introduction to Condition Monitoring

This chapter provides an introduction to condition monitoring, condition-based maintenance, and relevant signal processing. Section 2.2 is sourced from the pre-project [2].

2.1 Condition Monitoring

The process of monitoring a parameter of machinery in order to determine its condition while in operation is known as condition monitoring. The goal of condition monitoring is to detect impending failures, and has traditionally been implemented on equipment and systems where prevention of failures is of greatest importance. Condition monitoring is widely used across several industries, and both maintenance, operations and reliability engineers rely on condition data from systems to ensure that critical equipment and components operate efficiently and last as long as possible.

In the oil and gas industry, such applications often include critical rotating machinery, such as gas compressors, pumps and turbines. The ability to capture data that can be used for trend analysis and anomaly detection has improved as instrumentation tech-

nology, telecommunications technology, and analytical methods has advanced. Monitoring of basic sensor data and equipment on drilling rigs has been an important part of safe drilling operations for some time, and has permitted remotely located staff to study real-time data and to engage with offshore personnel. Analysis of acquired sensor data has helped increase efficiencies and improved risk management through better planning and execution [3].

Before implementing a condition monitoring system for a machinery, potential failure modes and their criticality need to be defined. Further, the detectability of the failure mode needs to be investigated, which involves definition of measured parameters and techniques. For the machinery being monitored, one or more measurement parameter and technique may be appropriate. Some parameters require only simple measurements of overall values. However, for current, voltage and vibration measurements, more advanced techniques such as spectral analysis might be required to reveal changes caused by faults [4].

2.2 Condition Based Maintenance

CBM is a maintenance strategy that utilizes real-time condition monitoring and diagnostics of impending failures to estimate the actual condition of the asset in question. Further, the CBM program recommends maintenance actions based on the condition monitoring data [5].

The key point of CBM is to assess reliability and maintenance based on a degradation model of the system in question. A relationship between system failure and amount of degradation makes it possible to use degradation models and data to make predictions and inferences about the failure time [6]. The assessments are based on data from various sources, and the condition monitoring system is one of those data sources.

Guidelines for CBM programs have been suggested in the community, and standards from standardization organizations such as ISO [4, 7] and IEEE [8] have been published. The architecture of CBM programs are somewhat varying, and is dependent on the organization, but the main attributes include sensing and data acquisition, data processing, diagnostics and prognostics, and maintenance decision reasoning.

2.2.1 Condition Based Maintenance of Subsea Systems

Subsea systems located in harsh environments are prone to degradation and failures. Failure of subsea equipment has big consequences, downtime, and operational expenditure. Hence, maintenance is of primary importance to ensure optimal productivity and safety. While topside systems rely on preventive maintenance and repairs, efforts should also be made to detect and diagnose problems of subsea systems prior to a maintenance operation.

The number of sensors installed on subsea production systems, such as chokes, pipelines, and wells, are constantly increasing. There is also a growing interest in the community to apply condition monitoring technology to new subsea processing systems, such as compressors, separators, and boosters [9]. Some CBM systems and programs have already been developed and implemented on a number of subsea systems to different degrees, including choke valves [10, 11] and Subsea Electronic Modules [12].

2.3 Signal Processing

Informative data from sensors and instrumentation should be processed and analyzed to extract useful information about the condition of the system under consideration. There are many different sensor technologies and signal processing techniques that can be used to make sense out of the myriad of information that can be collected. Raw data acquired from sensors needs pre-processing before further analysis, and there are numerous techniques that can be used to remove background noise, sensor noise, and human errors. After data acquisition, further techniques can be applied to extract useful information from the data. These techniques are broadly divided into time domain, frequency domain and time-frequency domain approaches.

Time domain approaches are based on the analysis of data as a function of time. Most techniques are based on the signal's statistical behavior. By studying the trends of these values over time, a deviation from standard system operating level may be detected. The principal advantage of time-domain techniques is that no data is lost prior to inspection. The disadvantage is, however, that there is often too much data for easy and

clear fault detection [13].

Spectral analysis, or frequency domain analysis, is probably the most widely used approach for fault detection of industrial systems and components. The general idea of such approaches is to transform the signal from time domain to frequency domain, to uncover the frequency components apparent in the time domain signal. This is illustrated in Figure 2.1. A defect in a given machine can generate a periodic signal with a unique characteristic frequency. These frequencies can be extracted and used for fault detection where time domain techniques would fail to make a simple analysis of the signal.

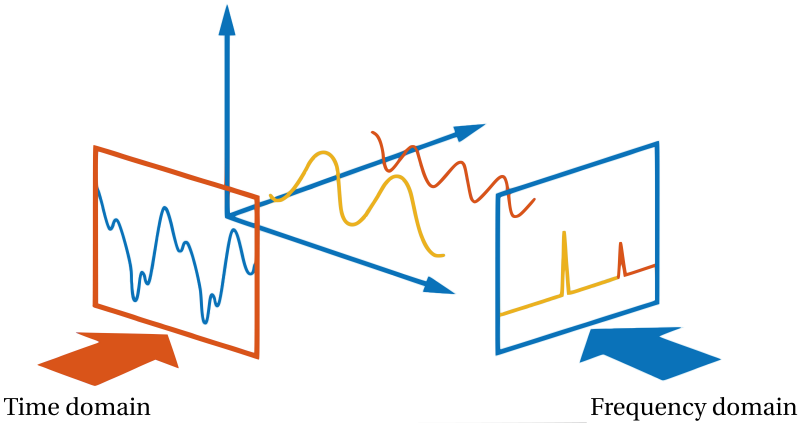

Figure 2.1: Time domain and frequency domain. Adapted from [14].

Spectral current analysis of electrical machines is commonly known as motor current signature analysis (MCSA), and utilizes the stator current measurement from the machine to provide a nonintrusive approach for detection of motor faults. The basis of MCSA is the reflection of mechanical torsional vibrations on the stator current, which are caused by various defects, such as rotor misalignment, bearing faults and airgap eccentricity [15]. In electromechanical drive trains, MCSA can also be utilized for detection of mechanical faults in other rotational components, such as gears [16]. As current sensors are usually designed into electric drives for control purposes, there is no extra sensor cost related to the implementation of this monitoring technique. Thus, MCSA serves as a cheap, non-intrusive condition monitoring technique with a potential for detection of several different faults.

Time-frequency analysis is used where both time- and frequency-domain approaches fail to detect faults accurately. By representing a signal by a time-frequency distribution, which shows the energy of the signal in the two-dimensional time-frequency space, it is possible to characterize signals with time-varying frequency content [17].

Chapter 3

The Blowout Preventer System

This chapter provides an introduction to the BOP system operation and construction, as well as new regulatory requirements for such systems. A description of the electrical BOP control system is also included. Section 3.1 is partially sourced from the pre-project [2].

3.1 Formation Kicks

The BOP system is a well barrier used during drilling and intervention of petroleum wells. It consists of several preventers and actuating components necessary to close or open the preventers, and acts as the wells secondary barrier, with the drilling mud being the primary barrier able to stop and control unintentional flow of formation fluid from the formation into the wellbore.

When drilling a well, a drill string is used to transmit the drilling mud and torque to the drill bit. The term drill string usually includes the drill pipe, bottom hole assembly, and any other tools that make the drill bit turn at the bottom of the wellbore. The drill string is deployed through the marine drilling riser, which is a pipe that extends from the drilling rig to the BOP. The BOP is locked to the subsea wellhead, with casing extending further down towards the reservoir. Drilling mud is used while drilling to keep

the hole from collapsing and to transport cuttings to the surface. The mud is pumped down through the drill string, and is returned in the annulus with cuttings. The column of drilling mud exerts downward hydrostatic pressure on the wellbore to counter opposing pore pressure from the formation being drilled, allowing drilling to proceed. A kick, however, occurs when the pore pressure in the formation is higher than the wellbore pressure, resulting in formation fluid flowing into the well.

When a kick is detected, actions are taken to close the wellbore by using one or more of the preventer(s) in the BOP, a procedure known as a shut-in. After the shut-in procedure is completed, a kill procedure must be done immediately to restore well control. There are several methods to kill a well, but the general idea is to circulate out any formation fluid in the wellbore by using a denser mud known as kill mud. The pressure in the well will increase until the total pressure exerted by the kill mud on the kicking formation equals the formation pore pressure.

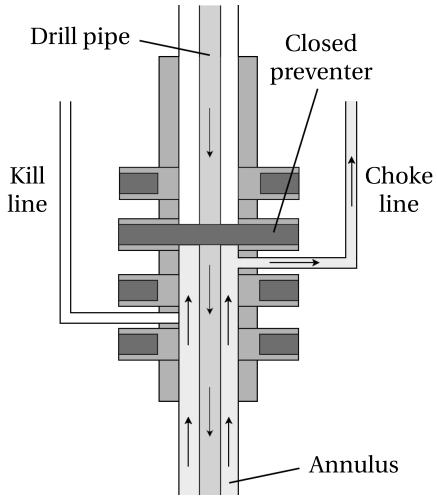

Figure 3.1: Killing a well by circulation through the choke line.

The kill mud is circulated into the wellbore by pumping it down the drill string, up the annulus and out through the choke line, which is a high-pressure pipe leading from an outlet on the BOP stack to topside. This process is illustrated in Figure 3.1. If circulation is not feasible, it may be possible to kill the well by pumping kill mud through the kill line, which is a pipe similar to the choke line. The difference is then that the dense mud is pumped into the top of the well, where it is possible to make use of the force

of gravity and wait for formation fluid to be removed from the annulus. If the shut-in and kill procedures does not restore well control, the BOP can shear the drill pipe and completely close and seal the well.

3.2 The Subsea BOP System Description

The BOP system can be located on the drilling rig, known as a surface BOP and common for fixed platform drilling rigs anchored directly onto the seabed, or on the seabed, known as a subsea BOP and common for floating submersible drilling rigs. Although the functionality of the two is similar, the following sections will only deal with the functionality and construction of subsea BOPs. A typical subsea BOP system is illustrated in Figure 3.2.

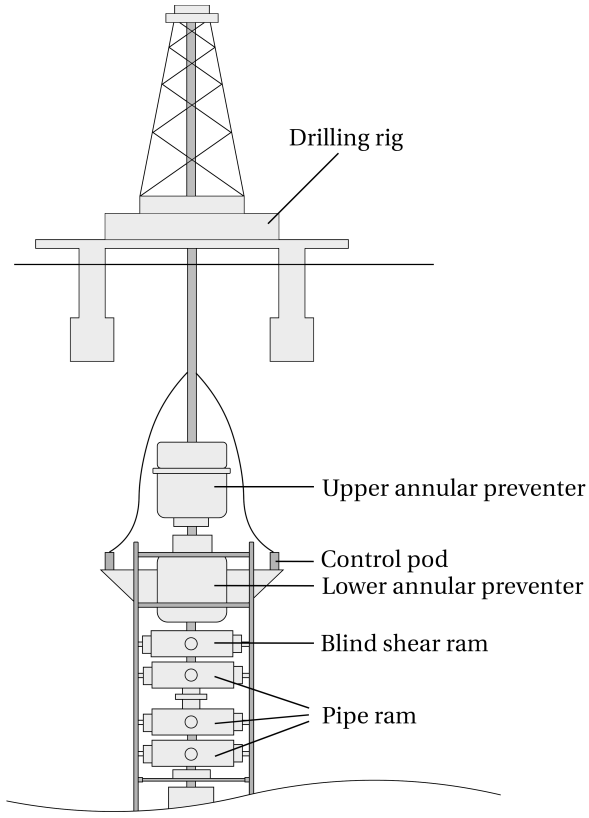

Figure 3.2: Typical architecture of a subsea BOP system.

3.2.1 Preventers

The preventers in a BOP can be categorized into two main types - annular preventers and ram preventers. The annular preventers are located in the Lower Marine Riser Package (LMRP), which is the upper part of the BOP. They are used to close the annulus during a shut-in, and resembles a large rubber doughnut that can be squeezed around the drill pipe.

The assembly of ram preventers is located in the lower part of the BOP, generally known as the BOP stack, which in addition to the ram preventers, includes a wellhead connector and the choke and kill lines. A ram preventer is essentially a pair of opposing steel blocks that through guide chambers, known as ram cavities, extend toward the center of the BOP wellbore to prevent returning flow when closed [18]. Ram preventers are of four common types; pipe, blind, shear and blind shear. The blind, pipe and shear rams are illustrated in Figure 3.3.

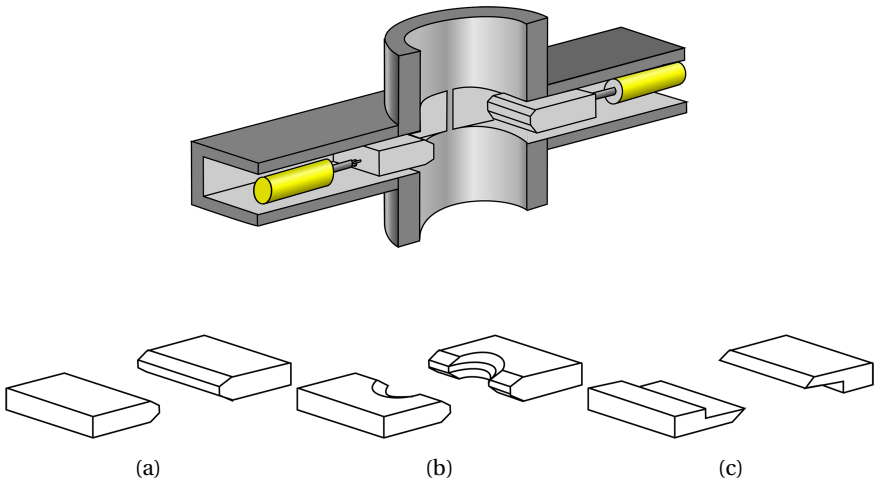

Figure 3.3: Simplified ram preventer design with different types of ram blocks. (a) Blind ram (b) Pipe ram (c) Shear ram. Adapted from [19].

The pipe ram has the same purpose as the annular preventer, closing off the annulus to prevent flow of formation fluid. The blind ram can close off and seal the well when the well does not contain a tubular (i.e. a drill pipe). The shear ram is able to shear/cut tubulars. The blind ram and the shear ram can be combined in one unit, known as the

blind shear ram, which is fitted with both shear ram blocks that can shear tubulars, and rubber seals that can seal off the well after the tubular is sheared.

3.2.2 Control System

The preventers in a conventional subsea BOP system are operated hydraulically by moving a piston back and forth. The hydraulic force used to activate the preventers is delivered from subsea accumulators mounted on the BOP. In order to deliver hydraulic fluid to the correct unit, a control system is used. The control system interacts with two redundant control pods mounted on the subsea BOP, which is an assembly of valves and regulators that respond to control signals to direct hydraulic fluid for operation of functions and components. Hydraulic fluid is stored in accumulators upstream of the control pods. From the control pods, the hydraulic fluid is directed to the subsea actuators via shuttle valves.

There are two kinds of BOP control systems in use today - pilot hydraulic (PH) control systems and electro-hydraulic multiplex (E/H MUX) control systems [20]. The main difference between the two is that the PH control system sends pilot hydraulic signals directly from the drilling rig to the control pods, whereas the E/H MUX control system sends electronic control signals to the control pods. Due to the nature of PH control systems, the response time increases with greater water depths. Therefore, to overcome signal delays, E/H MUX systems are used when water depths exceed 1500 meters [21].

3.3 New BOP Real-Time Monitoring Requirements

New requirements regarding condition monitoring and real-time data assessment will affect the operation of BOP systems in use on the U.S. Outer Continental Shelf (OCS), and thus set the standard for the industry on a worldwide basis. The Bureau of Safety and Environmental Enforcement (BSEE) is an agency under the United States Department of the Interior, and was established in the wake of the Deepwater Horizon tragedy in 2011, in order to separate regulatory responsibilities from activities concerning sales and revenue. BSEE's regulatory programs include developing and implementing regu-

lations and rules to promote safety, protect the environment, and conserve resources, such as the Well Control Rule (WCR).

The WCR [22], officially titled the "Oil and Gas and Sulfur Operations in the Outer Continental Shelf-Blowout Preventer Systems and Well Control", was published in its final version on April 29, 2016. The purpose of the rule is to prevent future well-control incidents, and aims to incorporate the latest industry standards that establish minimum baseline requirements for the design, manufacture, repair and, maintenance of blowout preventers. The rule imposes stricter requirements regarding controls of the maintenance and repair of BOPs, technical solutions and functionalities, reporting of failure data, and real-time monitoring (RTM) plans and capabilities for operations in the OCS.

Beginning in 2019, operators are required to use RTM during drilling operations, which will serve as a tool to improve safety and environmental protection. The rule is flexible in the sense that requirements and criteria for verifying compliance are not specifically stated. It is rather open to interpretation, and allows for flexibility for each operator to tailor their monitoring plan for each individual operation. As an example, RTM can be used to monitor and interpret data from areas such as BOP testing, and eventually used for condition monitoring and condition based maintenance of selected equipment.

There has been a lot of resistance from the drilling industry on many of the BSEE requirements in the WCR, and a new version of the rule was published on the 11th of May 2018 [23]. With respect to RTM, the latest rulemaking revises the applicable section (§250.724) by removing many of the prescriptive RTM requirements and moving towards a more performance-based approach. BSEE would still require the ability to gather and monitor real-time well data using an independent, automatic, and continuous monitoring system capable of recording, storing and transmitting data of the BOP control system, the well's fluid handling system on the rig, and the well's downhole conditions with the bottom hole assembly tools (if any tools are installed).

Based upon BSEE's evaluation of RTM since the publication of the original WCR, BSEE determined that the prescriptive requirements for how the data is handled may be revised to allow company-specific approaches to handling the data while still receiving the benefits of RTM. BSEE is specifically soliciting comments if there are alternative

ways to meet RTM provisions, or if there are alternative means to meet the purposes of RTM. BSEE expects operators to explain how they would carry out the requirements of the RTM plan on an individual company basis. BSEE revised this section to outline the RTM requirements and allow the operators to determine how they would fulfill those requirements. Further, they are soliciting comments about the appropriateness of utilizing RTM for workover, completion, and decommissioning operations, or whether RTM requirements should be limited to drilling operations.

3.4 BOP Test Requirements

BOP testing is carried out on a regular basis to ensure that its capability to prevent or minimize the release of wellbore fluids into or onto the ocean, earth or atmosphere is maintained. Test requirements are stated in NORSOK D-010 [24] and API R53 [25], and describes how and how often well barrier equipment should be tested. The test procedures involve pressure and function tests, where a pressure test is defined as a controlled pressurization and pressure monitoring of all or any part of a BOP system, including valves and sealing units, while a function test involves opening and closure of a preventer. Testing intervals are determined by local regulations. The NORSOK standard requires a pressure test every 14 days, and a function test every 7 days. The tests should be performed on all preventers in the BOP, including the shear rams. However, if there is a tubular in the BOP, the shear ram tests may be postponed and performed at a later time. Due to the regular test frequency, measurement data acquired during BOP testing can be analyzed and used for health indication for all or select units of the BOP system.

3.5 The All-Electric BOP Control System Design

ESD is in the process of developing a new BOP system with all-electric controls. A study conducted by MCS Kenny on behalf of BSEE [1] shows that control system failures are the most likely category of failure on BOP equipment, followed by failures on annular preventers and ram preventers. The use of hydraulics in the current PH and E/H MUX

control systems have limitations with respect to several potential leakage points, loss of energy potential of accumulators due to high ambient seawater pressure, and vulnerability with respect to contaminated hydraulic fluids. A change from electro-hydraulic to all-electric controls removes the common failure scenarios related to hydraulic systems, in addition to providing a possibility of reduced failure of the barrier elements by allowing for full control of applied force during operation of the preventers.

This section will further introduce the components and construction of the all-electric BOP system design.

3.5.1 Power

Electrical power will be provided by subsea Li-Ion batteries, charged from surface via electrical power cables. There will be several battery packages on both the LMRP and the lower BOP. The batteries will be placed in nitrogen-filled canisters with atmospheric pressure to provide protection. A Battery Monitoring System (BMS) provided by the battery supplier will be included in the system to allow for continuous monitoring of battery condition.

3.5.2 Data Communication

Data communication between the BOP-stack and topside may be carried out by optical fiber-cables. The communication system consists of an automation system and an emergency system, where the automation system will be used to interface actuator controls and subsea instrumentation, while the emergency system will ensure that all emergency operations are performed in a reliable manner. Dual Ethernet networks will be installed for both systems, and both systems will also feature separate acoustic data links, which can be used in case of an accidental cable break and/or a disconnection.

3.5.3 Actuators

Connectors and potentially also the annular preventers will be operated by electro-mechanical ring-piston actuators. However, ESD has taken over well barrier technol-

ogy developed by MHWirth, that was originally intended for hydraulic actuation and which shall now be adapted with electro-mechanical actuators and be prototyped and qualified. The preferred annular preventer solution uses radial actuation rather than a traditional axial actuation of an annular piston. The packing element is essentially a rubber annulus or doughnut reinforced by embedded steel inserts. The inserts are adhesively bonded to the rubber matrix, and the whole assembly is molded together as a unit. The metal inserts are arranged in a tangential array so that they can move radially inward together, to provide support for the rubber at any position from fully open to fully closed. The radial annular preventer will be developed with eight actuators that shall be driven in parallel, with synchronized stroke of the transmission elements in the actuator to actuate pusher plates that are linked to the metal inserts of the packing element. The radial annular preventer is illustrated in Figure 3.4.

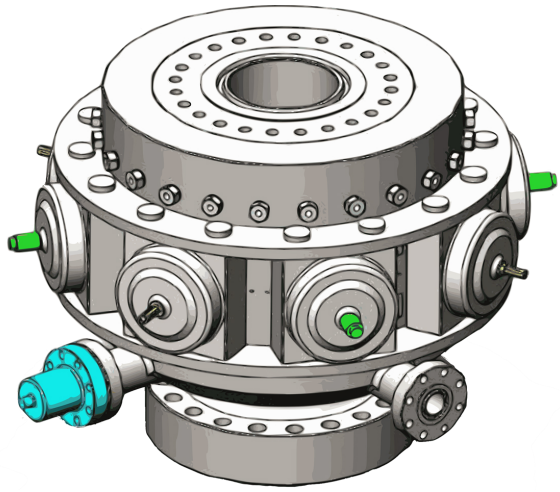

Figure 3.4: Radial annular preventer with hydraulic actuators. Figure provided by ESD.

The connector actuator consists of a PMSM whose rotor surrounds a ring nut, which is in threaded engagement with several rollers. Further, the rollers drive a ring-formed actuation element, acting as a roller screw. This design activates linear motion of the actuation element from a first to a second position by rotational motion of the motor. The ring-piston actuator used for the connectors is shown in Figure 3.5.

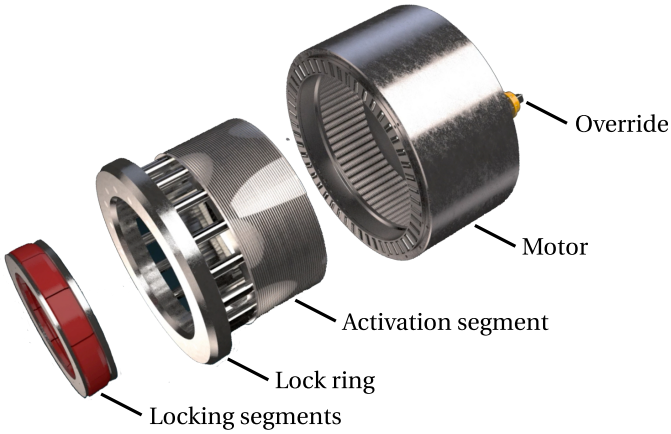

Figure 3.5: Ring-piston actuator. Figure provided by ESD.

The ram actuator design is based on two electric motors that each drives a planetary roller screw, via a mechanical transmission consisting of spur gears and planetary gear sets. The two planetary roller screws drive an actuating element, making it able to move from a first position to a second position along its longitudinal axis. The ram actuator design will be thoroughly presented in Chapter 4. All actuator designs will include a brake system that prevents actuator movement when power is lost.

3.5.4 Instrumentation and Condition Monitoring

The all-electric control system will enable control and condition monitoring on a higher level than what has previously been possible for subsea BOPs, in line with the new RTM requirements from BSEE as presented in Section 3.3. Planned instrumentation includes water sensors for detection of water ingress, accelerometers for vibration monitoring and detection of signal signatures that are present due to mechanical damages, temperature sensors for detection of temperature anomalies, and oil level sensors for monitoring oil levels. Rotary encoders will be monitoring the PMSM rotor and the shaft that connects the planetary gears and the planetary roller screw, both for motor control purposes and for speed and position monitoring of the rotor and screw. Current measurements will be carried out in the motor controller. As current and torque are proportional, the amount of current fed to the motor will give an indication of the torque

produced by the motor. Current sensors also allow for use of MCSA, which will serve as an invasive monitoring technique as discussed in Section 2.3. A draft instrumentation list for the actuators is given in Table 3.1.

Component	**Instrumentation**	**Purpose**
Motor housing	Water sensor	Detection of water ingress
Motor	Accelerometer	Detection of mechanical damage
Motor	Rotary encoder	Position and speed control/monitoring
Motor	Temperature sensor	Detection of temperature anomalies
Motor	Torque and current measurements from inverter	Position and speed control, current signature monitoring
Mechanical transmission	Accelerometer	Detection of mechanical damage
Mechanical transmission	Rotary encoder	Position and speed control/monitoring
Oil bath	Level sensor	Detection of oil level anomalies
Battery	BMS	Monitoring of available power and detection of anomalies

Table 3.1: Instrumentation overview of the electro-mechanical BOP actuators.

Chapter 4

The Electro-Mechanical Shear Ram Actuator

From here on, this thesis will focus on the shear ram actuator which is part of ESDs electrical BOP system design. This chapter describes the shear ram function and testing, the electro-mechanical shear ram actuator design and construction, and potential actuator faults that will be implemented in the shear ram actuator model in Chapter 5.

4.1 Function and Testing

If well control can not be restored during a well control event, the control function of last resort is to shear the tubular and seal the well. Shear ram is the general term for rams able to shear/cut tubulars in the wellbore. A blind shear ram is a combined closing and sealing unit in a BOP that is able to shear tubulars, followed by sealing the wellbore, as discussed in Section 3.2.1.

The shear rams are subject to regular function tests, as required by local regulations. As previously discussed in Section 3.3, NORSOK states that shear ram function tests should be performed every 7 days, but with permission to postponement if a tubular is present

in the wellbore. Although test procedures vary between operators and suppliers, the general idea is to close the shear ram on an empty hole (i.e. no tubular), before opening it again. During the test, the only counterforce exerted on the rams is the wellbore pressure that results from the weight of the drilling mud present in the wellbore, in addition to any externally applied pressure.

4.2 Shearing Device

The electro-mechanical shear ram actuator will be designed with the aim to provide the capability of shearing and sealing 9-inch drill collars. The required cutting force for this capability is not yet established, as it depends on several factors; of most importance is the performance of the shearing device used. A new GateRam™ shear ram technology will potentially lower the required cutting force. Based on preliminary studies, the targeted maximum output force for the dynamic load test will be in the order of 800 metric tons (MT). If this is validated, the design load of the device will most likely be 1,000 MT. The current design is based on the use of standard transmission element components and materials. For a new-build BOP, it may be possible to use larger roller screws and increase the output force to approximately 1,500 MT. Another way to increase the force capacity is to use stronger, non-standard materials in the transmission elements.

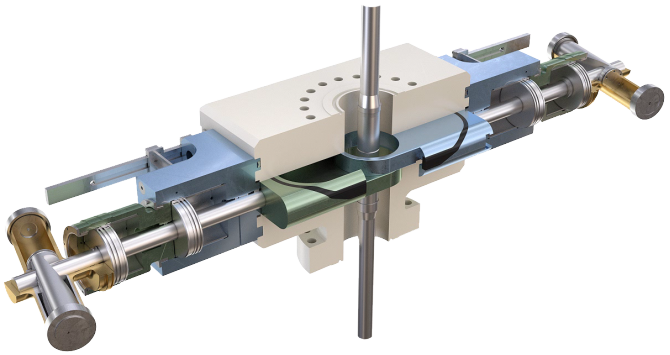

Figure 4.1: GateRam™ concept for 18 ¾ inch 15,000 psi BOP, with hydraulic actuators. Figure provided by ESD.

Figure 4.1 presents the GateRam™ concept for 18 ¾ inch 15,000 psi BOP with the orig-

inal design, including hydraulic actuators. The GateRam™ will centralize, cut and seal compressed pipe to the bore side, because it has a round hole, and the pipe will be forced to the center. Due to its cigar cutter design, it will have space inside when closed, which provides sufficient cutting capability to cut and seal 14-inch casing. Further, the GateRam™ has proven its capability to cut drill pipe joints in a test jig.

4.3 Actuator Design

A feasibility study for an 800 MT shear ram actuator, prepared by B. Cach for Transtech A/S on request from ESD in 2017 [26], in addition to the accompanying 3D model, is used as the principal mechanical design for the electro-mechanical shear ram actuator. The specifications presented in this section are mainly derived from this study, and through conversations with Magne Rød and Egil Eriksen in ESD.

The Transtech study describes an electric/gear-driven shear ram actuator capable of providing 800 metric tonne shearing force. In order to retain the ability of retrofit to any type of BOP, the overall dimensions are kept within present BOP-stack parameters. The design is based on a twin standard planetary roller screw that drives a load carriage which is fixed to a spindle that serves as the actuator nut. The twin standard planetary roller screw is driven by two identical, separate mechanical transmission systems, each located on either side of the load carriage. This will distribute the load to allow for smaller, standard roller screws to be used and reduce the overall size of the actuator, particularly the height to facilitate integration of the actuator with standard BOP equipment. Although the two power transmissions are separately driven by their respective motors, a manual override function that engages both transmissions simultaneously is included so that a remotely operated vehicle can take over the operation of the ram in case of power loss.

One PMSM is used to provide torque for each of the mechanical transmissions, which is a gearing arrangement consisting of spur gears and a double set of planetary gears. The output shafts of the planetary gears interfaces with each of the planetary roller screws, which drives its respective planetary roller screw nuts, which in turn drives the common load carriage. At last, the spindle that is fixed to the load carriage is connected to and

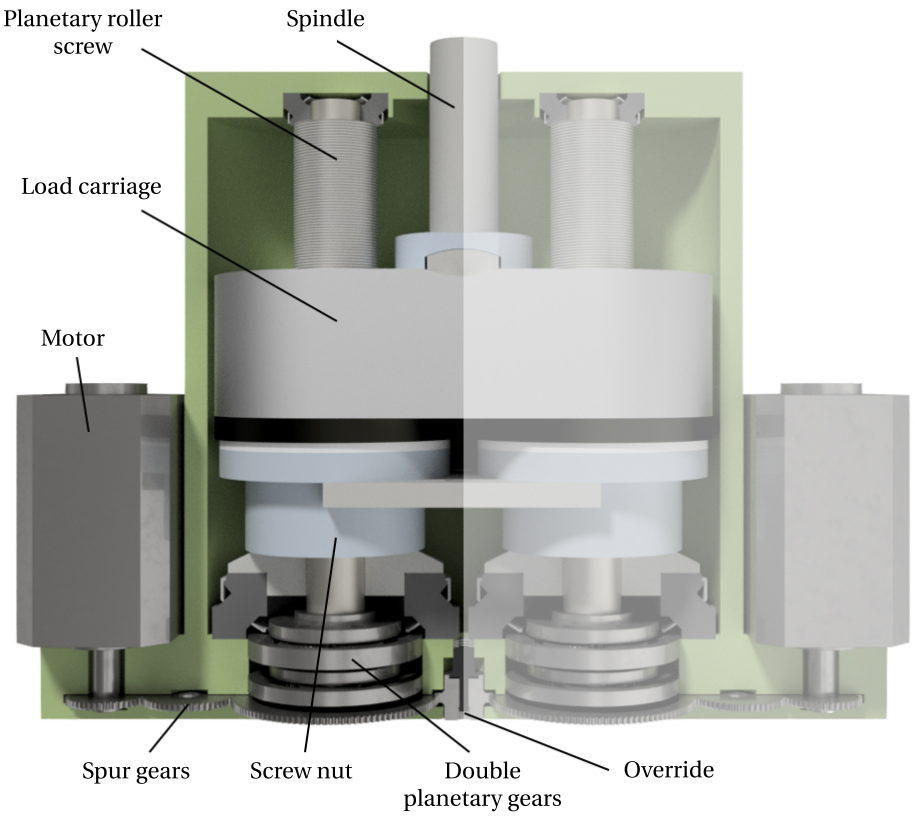

Figure 4.2: Detailed view of the electro-mechanical 800MT shear ram actuator. The left and right power transmissions are identical. The left transmission is highlighted in the figure. Adapted from [26].

drives the shear ram block back and forth. A detailed view of the actuator design is provided in Figure 4.2.

4.3.1 Motor and Drive

The ram actuator will be driven by two PMSMs, built to provide maximum torque for low speeds. The total motor output power is 155 kW, resulting in two 77.5 kW motors for each of the separate transmissions, with a nominal speed of ω_{nom} = 2200 rpm. The PMSM is an AC motor that has magnets mounted on or embedded in the rotor, rather than windings which is the case in the traditional AC induction motor. Such motors

have attracted increasing interest in recent years for industrial drive applications, due to its high efficiency, high torque density and simple controller configurations compared to the induction motor drives.

The rotor cores are usually made from steel, and the permanent magnets are made of Samarium-Cobalt (SmCo) or Neodymium-Iron-Boron (NdFeB) [27]. The magnets couple with the internal magnetic fields of the motor, generated by the electrical input to the stator. The PMSM rotates at synchronous speed, meaning that, at steady state, the rotational speed is a function of the frequency of the magnetic field produced by the stator windings [28]. A sketch of a PMSM is presented in Figure 4.3.

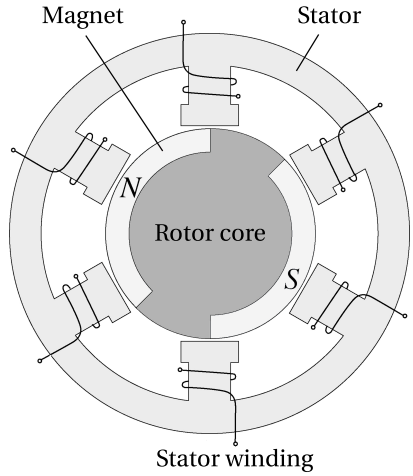

Figure 4.3: Permanent magnet synchronous motor sketch.

The motors will run on AC power provided by batteries via inverters and controlled by a motor drive, which is the electronics that control the speed and/or torque output of the motor. At the time of writing, no specifications were available for the motor drive in the electro-mechanical shear ram actuator. However, it is assumed that a sophisticated control method that allows for optimum control of torque and speed is chosen. For PMSMs, this is typically done by a control strategy known as vector control [27].

4.3.2 Mechanical Transmission

The mechanical transmission system consists of spur gears and a double planetary gear, in addition to a twin planetary roller screw. The spur gears are mounted in series, meaning that the input and output shafts are parallel to each other. The first spur gear is fixed to the rotor of the motor, and rotates at the same angular velocity as the rotor. There are a total of three spur gears for each of the two separate transmissions, so that the output gear rotates in the same direction as the motor wheel. The shear ram actuator spur gear arrangement is illustrated in Figure 4.4.

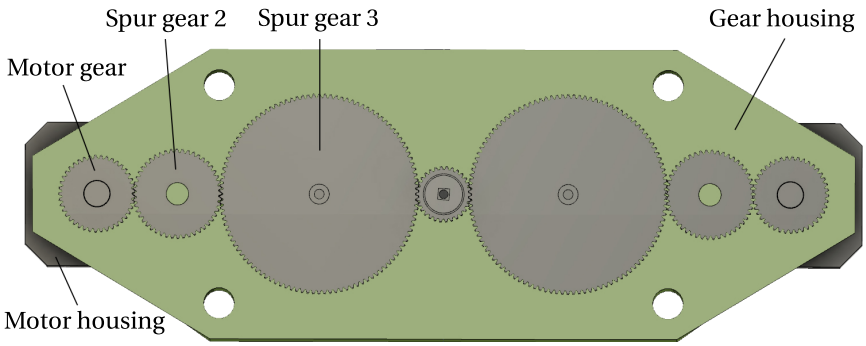

Figure 4.4: Rear view of the electro-mechanical shear ram actuator with the gear housing cover removed, showing the spur gear arrangement. Figure provided by ESD.

Planetary gears are used in a wide range of industrial applications, and can supply a lot of speed reduction and torque in a compact arrangement. Unlike spur gears, which rotates only around their own fixed centers, a planetary gear set has several planet gears that rotate around unfixed centers. Because the load in a planetary gear set is shared among multiple planet gears, the torque capability is greatly increased. A schematic of a planetary gear is shown in Figure 4.5.

All planetary and epicyclic gears have three bodies that are referred to as central members; the sun gear, the ring gear, and the planet carrier. There are multiple planet gears spaced around the central axis of rotation, which are simultaneously in mesh with both the sun gear and the ring gear. The planet gears are mounted to the planet carrier. In a standard planetary setup, where input power is delivered to the sun gear and the ring gear is fixed, the carrier delivers low-speed, high-torque output as the planet gears ro-

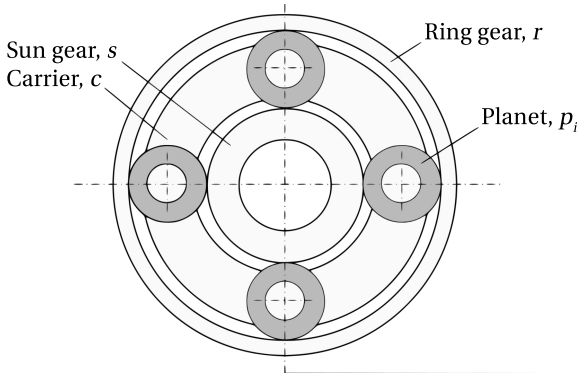

Figure 4.5: Planetary gear schematic. Adapted from [29].

tate around the sun gear. The planetary gears in the shear ram actuator is arranged so that the third spur gear is connected to the input sun gear of the first planetary gear, the output carrier of the first planetary gear is connected to the input sun gear of the second planetary gear, while the output carrier of the second planetary gear is connected to the planetary roller screw. The shear ram actuator planetary gear arrangement is illustrated in Figure 4.6.

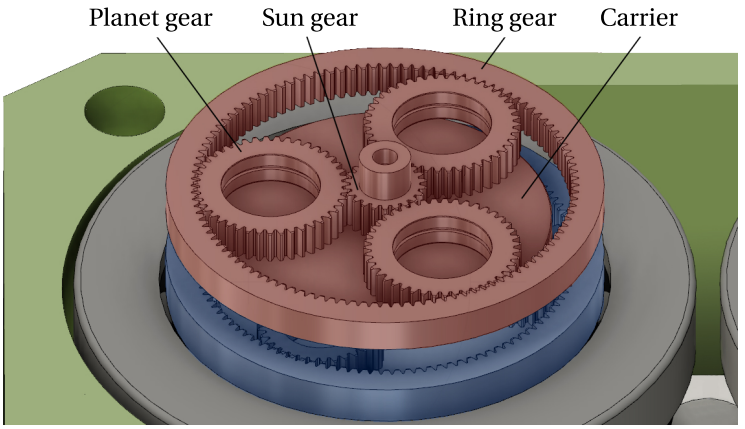

Figure 4.6: Cropped rear view of the electro-mechanical shear ram actuator with the gear housing removed, showing the planetary gear arrangement. The first planetary gear is highlighted in red color, and the second planetary gear is highlighted in blue color. Figure provided by ESD.

Both planetary gears have a three-planet arrangement that provides increased torque

output and speed reduction. The mechanical parameters for all gears are given in Table 4.1.

Component	Number of teeth	Base radius	Mass	Inertia
Spur gears				
Motor wheel	41	79 mm	2193 g	$6.8 \cdot 10^{-3}$ kgm^2
Wheel 1	48	93 mm	3214 g	$13.9 \cdot 10^{-3}$ kgm^2
Wheel 2	110	217 mm	18760 g	$441.7 \cdot 10^{-3}$ kgm^2
Input shaft		30 mm	3257 g	$1.5 \cdot 10^{-3}$ kgm^2
Output shaft		22 mm	281 g	$8.9 \cdot 10^{-5}$ kgm^2
1st Planetary gear				
Sun gear	21	30.5 mm	1278 g	$5.9 \cdot 10^{-4}$ kgm^2
Planet gear	42	62 mm	1718 g	$4.9 \cdot 10^{-3}$ kgm^2
Ring gear	109	171 mm	6682 g	$218 \cdot 10^{-3}$ kgm^2
Carrier		144 mm	13460 g	$139.6 \cdot 10^{-3}$ kgm^2
Output shaft		40 mm	864 g	$5.9 \cdot 10^{-4}$ kgm^2
2nd Planetary gear				
Sun gear	39	57.5 mm	1989 g	$4.9 \cdot 10^{-3}$ kgm^2
Planet gear	33	48.5 mm	1446 g	$2.6 \cdot 10^{-3}$ kgm^2
Ring gear	109	171 mm	8910 g	$291.1 \cdot 10^{-3}$ kgm^2
Carrier		144 mm	15260 g	$158.2 \cdot 10^{-3}$ kgm^2
Output shaft		90 mm	2679 g	$14.9 \cdot 10^{-3}$ kgm^2

Table 4.1: Mechanical parameters for the gear transmission in the electro-mechanical shear ram actuator.

A planetary roller screw is used in the mechanical transmission to convert rotational motion into linear motion. Its function is similar to the conventional ball and lead screws, but with rollers as the load transfer elements between the nut and screw. The use of rollers reduces friction between the contact surfaces, and allows for higher loads to be applied. The planetary roller screw's main components are the screw shaft, planetary rollers, and the nut. A planetary roller screw is illustrated in Figure 4.7.

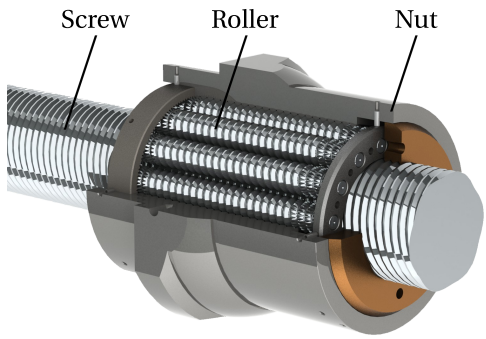

Figure 4.7: Planetary roller screw. Adapted from [30].

The proposed planetary roller screw to use in the electro-mechanical shear ram actuator is SKF's HRC180x25, which is a strong planetary roller screw designed for heavy loads. The diameter of the screw is 180 mm and the screw pitch is 25 mm [31].

4.4 Actuator Faults

System reliability and redundancy have been key elements in the design of the electro-mechanical shear ram actuator and the electrical BOP system in general, due to its critical safety feature during drilling operations. Motor drive reliability will be carried out either by having it meet the Safety Integrity Level 3 requirements[1], or by having fully redundant drives. The PMSMs will be produced with top quality from one end to the other. Motor power supply is ensured through continuous condition monitoring of the batteries by the supplied BMS. Doubled or over-sized bearings will be installed in the transmission system to reduce the risk of bearing failure.

Although the shear ram actuator is designed for high reliability, potential faults and failure modes should always be kept in mind. The most critical failure mode of the shear ram is the loss of ability to shear tubular and seal the wellbore. If one disregards external factors such as human errors, buckling drill pipe, too high wellbore pressure, and non-shearable tubulars, which are potential failure causes for this failure mode [33],

[1] Safety Integrity Level 3 is defined as a piece of hardware with Probability of Failure on Demand $\geq 10^{-4}$ to $< 10^{-3}$, and Probability of a Dangerous Failure Per Hour $\geq 10^{-8}$ to $< 10^{-7}$ [32].

failure to close the shear ram would be a result of electrical or mechanical actuator failure. In this study, due to the redundancy of the electronic components, attention is directed primarily towards the mechanical transmission system. The following subsections present the specific faults that are considered in this study and later implemented in the shear ram actuator model in Section 5.5.

Planetary Gear Faults

A gear crack, which may be hard to detect at first, can evolve under load and potentially lead to actuator breakdown at a critical time. Once initiated, crack propagation is accelerated by the effect of the tractive force, and may lead to catastrophic failures if not detected [34]. Traditionally, gear cracks in spur gears have been detected by the means of vibration monitoring, which is a well-developed technology, via accelerometers mounted directly on the gearbox housing [35]. Planetary gear sets exhibit unique vibration behaviors that invalidate diagnostic parameters developed for parallel spur gears. This is mainly due to the simultaneous meshing of planet gears, where vibrations with different phases couple with each other and cancel out characteristics that could potentially indicate a fault [36]. However, previous research of electro-mechanical drive trains has found that planetary gear tooth cracks appear at specific fault frequencies in the stator current spectrum [16, 37, 38].

Detection of such impending faults is of high importance. Thus, planetary gear faults are implemented in the shear ram actuator model, and investigated through analysis of several measurement parameters, including the stator current. Both specific tooth cracks and general gear wear are studied.

Motor Bearing Fault

Bearings are key components in most electrical machines, because they support the rotating motor shaft. In total, about 40-50% of all electric motor failures are bearing related [15]. Additionally, most mechanical faults in electrical drive trains are related to bearing damages [39]. Although the PMSM will be produced with top overall quality and over-sized bearings, this type of fault is included in the study due to its known

appearance in electric drivetrains. Traditionally, bearing faults have been detected by the use of vibration monitoring. However, MCSA has been successfully used for detection of bearing faults, providing a cheaper and non-intrusive method for fault detection [15].

Increased Shear Ram Block Friction

The use of electric motors to provide actuation force in the shear ram actuator makes it possible to provide detection of increased actuator output torque without any additional instrumentation, due to the proportionality between torque and motor current. The friction in the ram cavities may increase due to debris in the system, and will serve as a counterforce to the actuator. This counterforce will increase the torque required to close the shear ram, which leads to more power being consumed by the motors. Thus, current monitoring may be appropriate for detection of increased friction.

Chapter 5

Modeling of the Electro-Mechanical Shear Ram Actuator

The mathematical modeling of the electro-mechanical shear ram actuator is presented in this chapter. The model is based on one of the two actuator transmissions presented in Section 4.3. Further, the scenario to be modeled and simulated is a shear ram function test, where the actuator is set to close the shear ram. A model scheme is illustrated in Figure 5.1.

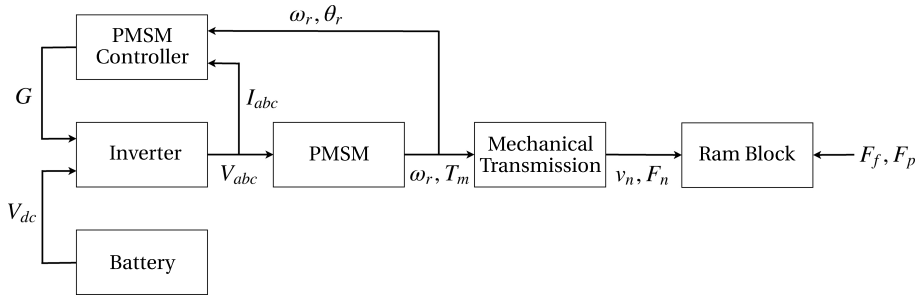

Figure 5.1: Electro-mechanical shear ram actuator model scheme.

5.1 Permanent Magnet Synchronous Motor

A mathematical model of the PMSM is derived using a two-phase motor in direct- and quadrature-axes, from here on referred to as dq-axes. This approach is desirable because of the simplicity obtained with only one set of two windings in the stator. The stator windings are considered to have equal turns per phase, and the rotor flux is assumed to be concentrated along the d-axis, while there is zero flux along the q-axis. Further, core losses are assumed negligible. The rotor has no windings, only magnets, and there is no external source connected to the rotor magnets. The magnets can be embedded in the rotor, known as an Interior PMSM or salient-pole PMSM, or mounted on the rotor, known as a Surface Mounted PMSM or non-salient-pole PMSM. A non-salient-pole PMSM is assumed in this model.

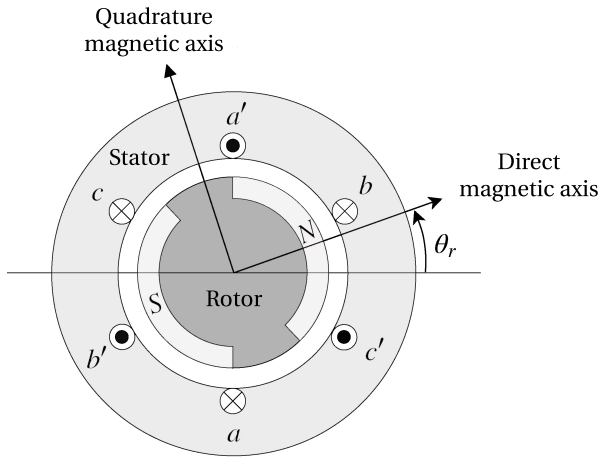

Figure 5.2: PMSM sketch with direct and quadrature axes.

The inductances in the stator windings are dependent on the rotor position, meaning that they vary as the rotor is revolving around its own axis. By looking at the entire system from the rotor, i.e. the rotor reference frame, the system inductance becomes independent of the rotor position, resulting in a simplification of the system. The transformation from the two-phase stationary reference frame, known as the $\alpha\beta$-frame, to the two-phase rotating rotor reference frame, known as the dq-frame, is achieved by replacing the actual stator and its windings with a fictitious stator that has the same number of turns for each phase and produces the equivalent magnetomotive force (MMF)

of the actual stator, rotating at an angular speed equal to the speed of the rotor. The relationships between the different frames are shown in figure 5.3 [40].

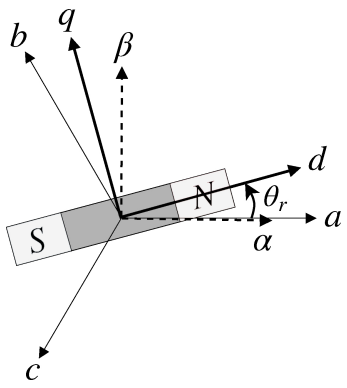

Figure 5.3: The relationship between the abc-, $\alpha\beta$- and the dq-frame.

The motor in the system considered is a three-phase motor. A model for the three-phase motor can be derived from the two-phase model by establishing an equivalence between the three and two phases. The equivalence is based on the equality of MMF produced and equal current magnitudes in the two-phase and three-phase windings. Thus, assuming that each of the three-phase windings has T_p turns per phase, and equal current magnitudes, the two-phase windings will have $\frac{3}{2}T_p$ turns per phase for MMF equality. Further, the dq-axes MMFs are found by resolving the MMFs of the three phases along the dq-axes. In total, these actions results in a transformation from the stationary three-phase abc-frame to the stationary two-phase $\alpha\beta$-frame, known as the Clarke transformation, and further, from the $\alpha\beta$-frame to the rotating two-phase dq-frame, which is known as the original Park transformation, given as,

$$T_{dq0} = \frac{2}{3}\begin{bmatrix} \cos\theta_e & \cos(\theta_e - \frac{2\pi}{3}) & \cos(\theta_e + \frac{2\pi}{3}) \\ -\sin\theta_e & -\sin(\theta_e - \frac{2\pi}{3}) & -\sin(\theta_e + \frac{2\pi}{3}) \\ \frac{1}{2} & \frac{1}{2} & \frac{1}{2} \end{bmatrix} \tag{5.1}$$

where θ_e is the angle between the d-axis of the two-phase frame and a-axis of the three-phase frame [27]. θ_e is also the rotor electrical angle defined as $\theta_e = N\theta_r$, where θ_r is the rotor mechanical angle, and N is the number of permanent magnet pole pairs. This transformation is generally known as the direct-quadrature-zero ($dq0$) transformation,

and can be used to define the relationship between the stator abc- and $dq0$-currents as,

$$\begin{bmatrix} i_d \\ i_q \\ i_0 \end{bmatrix} = T_{dq0} \begin{bmatrix} i_a \\ i_b \\ i_c \end{bmatrix} \tag{5.2}$$

The current component i_0 represents imbalances in the a-, b-, and c-phase currents as the zero sequence component of the current. The three-phase motor considered is assumed to have balanced windings and balanced inputs, meaning that the sum of the three-phase currents is zero and given as,

$$i_a + i_b + i_c = 0 \tag{5.3}$$

leading to a zero sequence current of zero value,

$$i_0 = \frac{1}{3}(i_a + i_b + i_c) = 0 \tag{5.4}$$

The d- and q-axes stator voltages v_d, v_q can be written in terms of the flux linkages and resistive voltage drops in the rotor reference frame as,

$$\begin{bmatrix} v_d \\ v_q \end{bmatrix} = \begin{bmatrix} -\omega_r L_q & R_s + L_d \frac{d}{dt} \\ R_s + L_q \frac{d}{dt} & \omega_r L_d \end{bmatrix} \begin{bmatrix} i_d \\ i_q \end{bmatrix} + \begin{bmatrix} \omega_r \lambda_m \\ 0 \end{bmatrix} \tag{5.5}$$

where R_s is the resistance of each of the stator windings, L_d and L_q are the d- and q-axes inductances, and λ_m is the rotor flux linkages that link the stator [27].

The electromagnetic torque determines the mechanical dynamics of the motor, such as the rotor position and speed, and is the most important output variable of the model. The electromagnetic torque T_e is given as,

$$T_e = -\frac{3}{2} N(\lambda_m i_q + (L_d - L_q) i_d i_q) \tag{5.6}$$

For a non-salient-pole PMSM, with equal d- and q-axes inductances, the expression simplifies to,

$$T_e = -\frac{3}{2}N(\lambda_m i_q) \tag{5.7}$$

The relationship between rotor position θ_r and rotor angular velocity ω_r is given as,

$$\frac{d\theta_r}{dt} = \omega_r(t) \tag{5.8}$$

The electrical supply frequency of the motor f_e is described by,

$$f_e = \frac{\omega_r}{2\pi}N \tag{5.9}$$

The equations listed above (5.5)-(5.9) gives a complete mathematical model of the PMSM. The PMSM is represented in the Simulink model by a custom Simscape block written in the Simscape language. The Simscape code is included in Appendix A Listing A.1.

For the PMSM model, the parameters N, R_s, L_d, L_q and λ_m needs to be defined. The motor to be used in the electro-mechanical shear ram actuator, which is presented in Section 4.3.1, has a rated output power of 77.5 kW. No further motor parameters were provided, so the parameters used in the following simulations are obtained from [41], where motor parameters for a 75 kW PMSM are presented. The parameters are given in Table 5.1.

Number of pole pairs	N	6
Stator resistance	R_s	12.69 mΩ
Magnetic flux linkage	λ_m	0.104 Wb
d-axis inductance	L_d	0.171 mH
q-axis inductance	L_q	0.391 mH

Table 5.1: PMSM parameteres used in simulations.

5.2 Motor Drive

A motor drive is necessary to achieve desired motor behavior. High-performance motor control is characterized by smooth rotation over the entire speed range, full torque control, and fast acceleration and deceleration. To achieve such control for PMSMs, vector control techniques are applied. The freedom to change and control stator currents in a PMSM, not only in magnitude and frequency, but also in phase, bestows a control equivalent to that of the separately excited DC machine control [27]. The separation of control for torque and mutual flux from each other, termed decoupling or vector control, is a popular control strategy applied to PMSMs. Vector control techniques are also referred to as field-oriented control (FOC). The flux is controlled by the field current alone, and may be termed as the flux-producing current. Keeping the field current constant at any time instant, and hence the flux constant, the torque is controlled independently by the armature current alone, which may be termed as the torque-producing current [40].

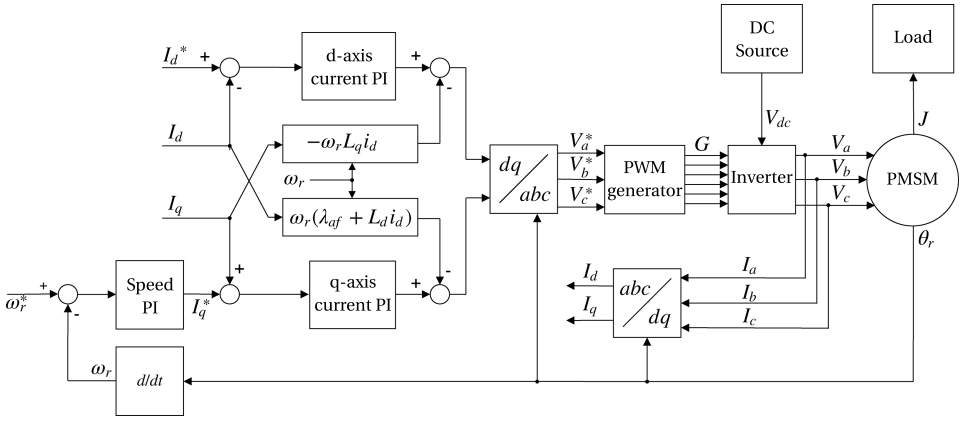

Figure 5.4: PMSM control scheme.

The PMSM control scheme is presented in figure 5.4. The controller is based on a current-controlled voltage source inverter structure. There are a total of three proportional-integral (PI) controllers in the system - one speed controller and two current controllers. The current control loops are arranged in the two-phase synchronously rotating rotor reference dq-frame, aligned with rotor flux (also rotor position θ_r), while the rotor po-

sition and speed operates in the stationary reference $\alpha\beta$-frame.

The rotor reference angular velocity ω_r^* is compared to the measured angular velocity ω_r, where the error is amplified in the speed PI controller to nullify the error and to generate an electromagnetic torque reference, T_e^*. Torque is related to the speed by the mechanical equation of the motor, given as,

$$\frac{d\omega_r}{dt}(t) = \frac{1}{J_m}\left(T_e(t) - T_m(t) - B_m\omega_r(t)\right) \tag{5.10}$$

where J_m is the inertia of the motor, T_m is the mechanical torque of the output shaft, B_m is the viscous friction coefficient. Further, the reference torque is converted to a q-axis current reference i_q^* by the use of equation (5.7).

The d- and q-axes have their own respective current PI controllers. While the q-axis current reference is obtained as previously explained, the d-axis current reference is set to zero because there is no flux weakening operation in this control scheme. Flux weakening operation is a technique used to obtain motor speeds above synchronous speed [27].

The dq-axes current references are compared to the measured dq-transformed abc-currents fed to the motor, and controlled in their respective controllers. Feed-forward compensation is used according to equation (5.5) to enhance system performance. The current PI controllers output reference voltages v_d^* and v_q^*, which are transformed from the dq-frame to the abc-frame by the inverse $dq0$-transformation, and fed to a PWM generator which generates gate signals for the inverter.

Tuning of the PI controllers are carried out with the following method as proposed by [42],

$$\alpha_i = \frac{2\pi f_{sw}}{10} \tag{5.11a}$$

$$\alpha_\omega = \frac{\alpha_i}{10} \tag{5.11b}$$

$$K_{pd} = \alpha_i L_d \tag{5.11c}$$

$$K_{id} = \alpha_i R_s \tag{5.11d}$$

$$K_{pq} = \alpha_i L_q \tag{5.11e}$$

$$K_{iq} = \alpha_i R_s \tag{5.11f}$$

$$K_{p\omega} = \alpha_\omega J \tag{5.11g}$$

$$K_{i\omega} = \alpha_\omega B \tag{5.11h}$$

where α_i and α_ω are the current and speed controller bandwidths, K_{pd}, K_{pq}, $K_{p\omega}$ and K_{id}, K_{iq}, $K_{i\omega}$ are the proportional and integral terms for the respective controllers, and f_{sw} is the pulse width modulation (PWM) switching frequency.

All controllers are designed with output saturation limits, which are implemented to take care of the torque and voltage limits of the system. The torque limits are determined by the motor ratings, while the voltage limits are determined by the capability of the power electronics that supply the voltage, with a maximum value of V_{max} and a minimum value of $-V_{max}$. For an inverter-fed PMSM vector controlled in the dq-frame, the maximum voltage is given as,

$$V_{max} = \sqrt{\frac{2}{3}} V_{dc} \tag{5.12}$$

By implementing voltage limits, the true voltage v is a limitation of the ideal voltage, so that the current control loop contains a nonlinearity. This leads to a common controller problem known as integral windup. When a relatively large change in set point occurs, the integral term of the PI controller keeps accumulating the control error while the output voltage is limited to the maximum voltage output. When the signal reaches its reference, it will continue to increase due to the error windup, leading to an overshoot until the windup has been worked off by accumulation of negative control error [42]. This problem is prevented by using an anti-windup technique known as back-calculation in the controllers.

The controllers are implemented in the Simulink model by using the Simulink block *PID Controller* with discrete-time settings, which includes output saturation and anti-windup. To achieve PI performance, only the proportional and integral terms are activated. The controllers generate a voltage reference signal in the dq-frame, which is

transformed to the abc-frame by the inverse $dq0$-transformation

The PWM gate signal generation is conducted by the Simscape block *PWM Generator (Three-phase, Two-level)*, which controls switching behavior for a three-phase, two-level power converter. It calculates on- and off-gating times based on the outputs of the current controllers, and uses the gating times to generate six switch-controlling pulses and modulation waveforms [43]. The six switch-controlling pulses are then fed to the inverter.

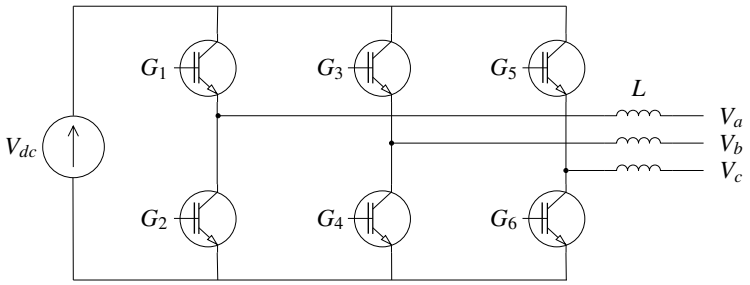

Figure 5.5: Three-phase inverter. G_1-G_6 are the PWM control pulses.

The inverter consists of six power semiconductor devices which convert DC power to AC power. A sketch of the inverter is presented in Figure 5.5. In the Simulink model, the semiconductor devices are represented as insulated-gate bipolar transistors (IGBT). The Simscape block *IGBT* is used for this purpose. The inverter consists of three single-phase inverter switches each connected to one of the three motor terminals. Each switch-controlling pulse from the PWM generator controls one of the IGBTs in the inverter. The operation of the three switches is coordinated so that one switch operates at each 60-degree point of the fundamental output waveform.

The inverter is supplied by a DC voltage source, which represents the battery in the actuator design. The voltage source is represented in the Simulink model by the use of the Simscape block *DC Voltage Source*. The motor drive parameters used in simulations are presented in Table 5.2.

DC link voltage	V_{dc}	800 V
Speed reference	ω_r^*	2173 rpm
Torque limit	T_{max}	325 N m
PWM swiching frequency	f_{sw}	10 kHz

Table 5.2: Motor drive parameters used in simulations.

Figures of the motor drive model are included in Appendix B Figures B.1-B.4.

5.3 Mechanical Transmission

This section presents the mathematical models used to describe the spur gears, planetary gears and roller screw in the actuator's mechanical transmission.

5.3.1 Spur Gears

The spur gears in the shear ram actuator is represented as an ideal, non-planetary, fixed gear ratio gear box. A reduction spur gear with gear ratio R_{sg} is described by,

$$\omega_{sg,out} = R_{sg}\omega_{sg,in} \tag{5.13}$$

where $\omega_{sg,in}$ is the angular velocity of the input side of the gear, and $\omega_{sg,out}$ is the angular velocity of the shaft on the output side of the gear [44]. The spur gear ratio R_{sg} is described by the number of teeth of the driving (input) and driven (output) gear as,

$$R_{sg} = \frac{N_{sg,in}}{N_{sg,out}} \tag{5.14}$$

where $N_{sg,in}$ and $N_{sg,out}$ is the number of teeth on the driving and driven gear, respectively. Further, the torque relation between the input torque $T_{sg,in}$ and the output torque $T_{sg,out}$ is found by comparing input and output power of the gear. If the gear is assumed to be lossless, so that the input power is equal to the output power, thus,

$$T_{sg,in}\omega_{sg,in} = T_{sg,out}\omega_{sg,out} \tag{5.15}$$

which gives,

$$T_{sg,out} = T_{sg,in}R_{sg} \tag{5.16}$$

For a spur gear arrangement that consists of more than two gears, as in the shear ram actuator, equation (5.14) still applies, meaning that the total gear ratio is given by the number of teeth of the motor gear and the third spur gear (see Section 4.3.2). The spur gears are represented in the Simulink model by the Simscape block *Gear Box*. The input torque and velocity are provided by the mechanical torque and angular velocity of the PMSM rotor, T_m and ω_r.

5.3.2 Planetary Gears

To enable investigation of planetary gear faults, a more detailed model is desirable. A lumped-parameter dynamic planetary gear model has been extensively used for research of the planetary gear dynamics, and several variations have been proposed in literature [29, 45, 46, 47]. The lumped-parameter dynamic model includes all central members (sun gear (s), ring gear (r), and carrier (c)), and an arbitrary number N_p of planet gears (p_i, $i = 1,2,...,n_p$).

The model used in this study is a purely torsional non-linear dynamic model that includes time-varying mesh stiffnesses. A purely torsional model neglects the transverse degrees of freedom, meaning that each member is assumed to move in the torsional θ direction only.

The planets are assumed to be equally spaced, located at an angle $\Theta_{p_i} = (i-1)\frac{2\pi}{n_p}$ with respect to the first planet p_1 located at $\Theta_{p_1} = 0$. Each member j ($j = s,c,p_i$) of the model is treated as a rigid body of polar mass moment of inertia J_j, base radius r_{bj} and torsional displacement θ_j. External torques T_j are applied to the sun and carrier to represent input and output torque values. Further, the flexibilities of the gear teeth at each gear mesh are modeled as time-varying mesh stiffness functions, K_{sp_i} and K_{rp_i},

acting along the gear line of action. The damping dynamics at the gear meshes are represented by viscous gear mesh damping elements, C_{sp_i} and C_{rp_i}. Transmission errors due to manufacturing and installation errors are neglected in this study.

Accordingly, equations of motion for a single stage planetary gear with fixed ring gear are expressed as,

$$J_s\ddot{\theta}_s + r_{bs}\sum_{i=1}^{3}\left(C_{sp_i}\dot{X}_{sp_i}(t)\right) + r_{bs}\sum_{i=1}^{3}\left(K_{sp_i}X_{sp_i}(t)\right) = T_s \tag{5.17a}$$

$$\begin{aligned}\left(J_c + M_p {r_{bc}}^2\right)\ddot{\theta}_c - r_{bc}\sum_{i=1}^{3}\left(C_{sp_i}\dot{X}_{sp_i}(t)\right) - r_{bc}\sum_{i=1}^{3}\left(C_{rp_i}\dot{X}_{rp_i}(t)\right)\\ - r_{bc}\sum_{i=1}^{3}\left(K_{sp_i}X_{sp_i}(t)\right) - r_{bc}\sum_{i=1}^{3}\left(K_{rp_i}X_{rp_i}(t)\right) = T_c\end{aligned} \tag{5.17b}$$

$$\begin{aligned}J_p\ddot{\theta}_{p_i} + r_{bp}C_{sp_i}\dot{X}_{sp_i}(t) - r_{bp}C_{rp_i}\dot{X}_{rp_i}(t)\\ + r_{bp}K_{sp_i}(t)X_{sp_i}(t) - r_{bp}K_{rp_i}(t)X_{rp_i}(t) = 0\end{aligned} \tag{5.17c}$$

where the relative gear mesh displacements are defined as,

$$X_{sp_i}(t) = r_{bs}\theta_s - r_{bc}\theta_c + r_{bp}\theta_{p_i} \tag{5.17d}$$

$$X_{rp_i}(t) = -r_{bc}\theta_c - r_{bp_i}\theta_{p_i} \tag{5.17e}$$

Equations (5.17a)-(5.17e) are often expressed in matrix form as,

$$\boldsymbol{M}\ddot{\boldsymbol{\theta}}(t) + \boldsymbol{C}\dot{\boldsymbol{\theta}}(t) + \boldsymbol{K}\boldsymbol{\theta}(t) = \boldsymbol{F}(t) \tag{5.18}$$

where $\boldsymbol{M}$ is the mass matrix, $\boldsymbol{C}$ is the damping matrix, $\boldsymbol{K}(t)$ is the time-varying gear mesh stiffness matrix, $\boldsymbol{F}(t)$ is the external applied torques vector, and $\boldsymbol{\theta}(t)$ is the degrees of freedom vector which contains the coordinate for torsional motion for each gear.

The time-varying mesh stiffness functions can be represented as square waveforms that

vary as the driven gear rotates. The change from the high and low state of the square wave is due to the change of contact between the driven and opposing gear, from single tooth pair in contact to double tooth pair in contact. Hence, the period of one gear mesh consists of two parts, the single tooth pair contact period τ_s and the double tooth pair contact period τ_d, as illustrated in Figure 5.6 [47, 48]. The single tooth pair and double tooth pair contact periods are assumed to be equal.

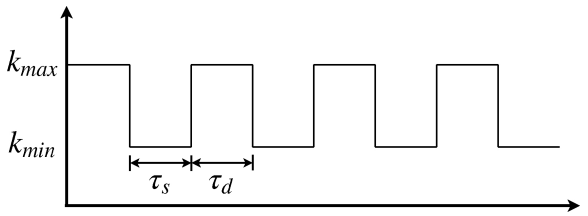

Figure 5.6: Illustration of the time-varying gear mesh stiffness function.

The square waveform can be represented as a Fourier series as,

$$K_{jp_i}(t) = k_0 + \sum_{n=1}^{\infty} a_n cos(2\pi n f_m t) \tag{5.19a}$$

$$k_0 = 2(k_{max} - k_{min}) \tag{5.19b}$$

$$a_n = \sum_{n=1}^{\infty} \frac{k_0}{n\pi} sin\left(\frac{n\pi}{2}\right) \tag{5.19c}$$

where $j = s, r$, and k_{max} and k_{min} are the maximum and minimum values of mesh stiffness. $k_{max} = 5 \cdot 10^8$ Nm/rad and $k_{min} = 3 \cdot 10^8$ Nm/rad are values commonly used in literature, and are assumed to be equal for both the sun-planet and the ring-planet meshes [16, 47, 48]. f_m is the gear mesh frequency described by,

$$f_m = \frac{N_s \omega_s}{2\pi} \tag{5.20}$$

where ω_s is the angular velocity of the sun gear, and N_s is the number of sun gear teeth. The mesh frequency is equal for both the sun-planet and ring-planet meshes.

The viscous gear mesh damping elements can be represented as,

$$C_{sp_i}(t) = 2\xi\sqrt{\frac{K_{sp_i}(t)J_sJ_{p_i}}{r_{bs}^2J_{p_i} + r_{bp_i}^2J_s}} \tag{5.21a}$$

$$C_{rp_i}(t) = 2\xi\sqrt{\frac{K_{rp_i}(t)J_{p_i}}{r_{bp_i}^2}} \tag{5.21b}$$

where ξ is the gear damping rate, which is assumed to be 5 %. To simplify the damping elements, $K_{jp_i}(t)$ can be substituted by the average gear mesh stiffness value $\bar{K}_{jp_i}$, given as,

$$\bar{K}_{jp_i} = \frac{k_{max} - k_{min}}{2} + k_{min} \tag{5.21c}$$

The planetary gears are represented in the Simulink model by custom Simscape blocks written in the Simscape language. The code is included in Appendix A Listings A.3-A.4. The simulation parameters used for the gear models are presented in Table 4.1. From here on, the parameters related to the 1st and 2nd planetary gear are presented with subscript 1 and 2, respectively.

5.3.3 Planetary Roller Screw

The rotational-translational motion conversion is performed by a planetary roller screw in the electro-mechanical shear ram actuator design. However, to simplify the model, the rotational-translational conversion is modeled by the means of a lead screw (or power screw), which has the same principal functionality as the planetary roller screw, but without the rollers.

In this model, power is transmitted by the use of screw and nut threads, represented as a threaded rotational-translational gear. In Figure 5.7, a lead screw with single thread having mean diameter d_{sc}, pitch p_{sc}, lead angle γ_{sc} is loaded by the axial force F_n. The thread lead L_{sc} is defined as the translational displacement of the nut for one turn of the screw, described by,

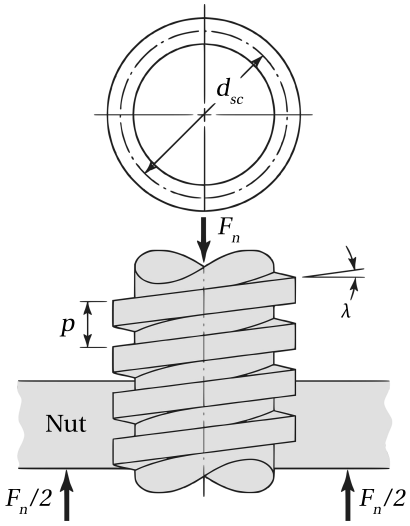

Figure 5.7: Portion of a lead screw. Adapted from [49].

$$L_{sc} = \frac{\tan \gamma_{sc}}{\pi d_{sc}} \tag{5.22}$$

The kinematic relationship defining a lead screw is simple, where the product of the angular rotation of either the screw or the nut and the thread lead L_{sc} results in the translation of the other element. The same kinematic relationship defines the angular and translational velocities. The relationship is described by,

$$x_n = \frac{\theta_{sc} L_{sc}}{2\pi} \tag{5.23a}$$

$$v_n = \frac{\omega_{sc} L_{sc}}{2\pi} \tag{5.23b}$$

where x_n is the linear translation of the nut, θ_{sc} is the angular rotation of the screw, v_n is the translational velocity of the nut, and ω_{sc} is the angular velocity of the screw. Further, the torque-force transfer between the screw and the nut is given as,

$$f_n = \frac{2\pi T_{sc}}{L_{sc}} \eta_{sn} \tag{5.24}$$

where F_n is the axial force acting on the nut, T_{sc} is the torque required to move the load, and η_{sn} is the screw-nut efficiency [49]. In practice, the efficiency is dependent on threading geometry and contact friction forces, but is assumed to be constant in this model.

The lead screw is represented in the Simulink model by use of the Simscape block *Lead-screw*. The parameters used in simulations are based on the screw introduced in Section 4.3.2, and are presented in Table 5.3.

Thread lead	L_{sc}	25 mm
Screw diameter	d_{sc}	180 mm
Screw-nut efficiency	η_{sn}	0.84

Table 5.3: Roller screw parameters.

5.4 Shear Ram Block

The shear ram block refers to the shearing device driven by the electro-mechanical shear ram actuator. The model is based on Newton's law of a block of mass m_r sliding in a ram cavity due to an external force F_a applied from the shear ram actuator, which is assumed to be the output axial force of the planetary roller screw F_n. A friction force between the contact surfaces F_f opposes the motion of the ram block. Additionally, the wellbore pressure present in the BOP provides another opposing force of the ram block motion. The forces acting on the ram block are illustrated in Figure 5.8. It should be noted that pressure compensation of the actuator is not considered in this model, which could potentially lead to changes in the system forces.

5.4.1 Friction

Model-based friction compensation is used in models of physical systems to account for the opposing reaction force between two surfaces in contact, known as the friction force. The friction force is dependent on a number of factors, such as contact geometry, surface material properties, displacement and relative velocity.

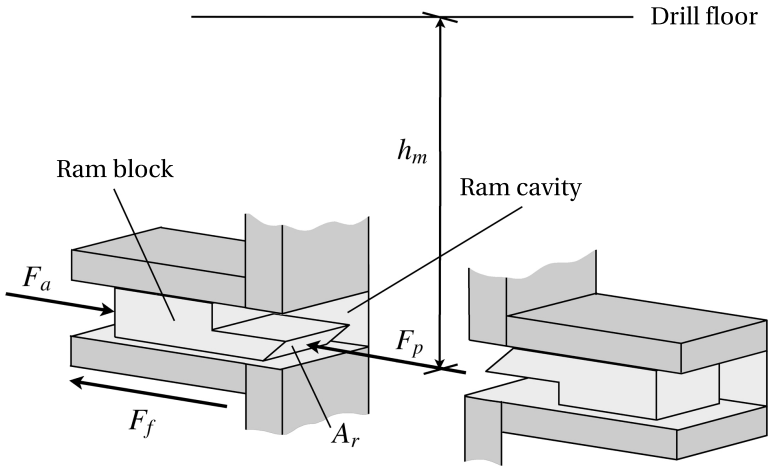

Figure 5.8: Simplified sketch of the forces acting on the ram blocks in the ram cavities.

The classical model of friction where the friction force is proportional to the load, opposes the motion, and is independent of contact area is known as Coulomb friction. The Coulomb friction model is given by,

$$F_f = F_c \text{sgn}(v_r), \qquad v \neq 0 \tag{5.25a}$$

$$F_c = \mu_c \frac{F_N}{2} \tag{5.25b}$$

where μ_c is the Coulomb friction coefficient, v_r is the velocity of the mass, and $F_N = \frac{m_r g}{2}$ is the applied load [44]. The division factor of 2 is included because only one of the two actuator transmissions is considered in this model. The opposing force is assumed to be evenly distributed on the two transmissions.

This model is not defined at zero velocity, however, the Coulomb model can be extended to be valid at zero velocity using Karnopp's friction model,

$$F_f = \begin{cases} \text{sat}\,(F_a, F_c)\,, & v = 0 \\ F_c \text{sgn}(v), & else \end{cases} \tag{5.26a}$$

In this formulation, the Coulomb friction force is a function of the velocity. The velocity remains equal to zero as long as the applied force F_a is less than F_c in magnitude. The

saturation function $\text{sat}(F_a, F_c)$ is defined by,

$$\text{sat}(F_a, F_c) = \begin{cases} F_a, & |F_a| \leq F_c \\ F_c \text{sgn}(F_a), & |F_a| \geq F_c \end{cases} \tag{5.26b}$$

However, the Coulomb model does not account for static friction, or stiction, which is the pre-sliding friction force between two surfaces that are not moving relative to each other. According to the stiction model, the friction force is larger in magnitude for zero velocity than for a non-zero velocity. Thus, the system sticks if $v_r = 0$ and $|F_f| < F_s$, and it breaks away if $|F_f| = F_s$, where $F_s = \mu_s F_N$ is the stiction force, and $\mu_s > \mu_c$ is the stiction coefficient [44].

Viscous friction is also present in fluid lubricated contacts between solids, and takes hydrodynamic effects into account. A phenomenon used in viscous friction models is the Stribeck effect. This effect is described by the Stribeck curve, which shows how the viscous friction between two lubricated surfaces changes with increasing velocity, where the friction force initially decreases to a minimum before increasing again. A static model for the Stribeck effect can be described by,

$$F_f = \left[F_c + (F_s - F_c)\, e^{-(v_r / v_s)^2} \right] \text{sgn}(v_r), \qquad v_r \neq 0 \tag{5.27}$$

where v_s is the characteristic velocity of the Stribeck friction [50]. It should be noted that parameter identification of v_s is usually based on curve fitting to experimental data, and is very difficult to estimate.

Karnopp's friction model (5.26) can be extended by including the Stribeck effect (5.27), so that the friction force is given by,

$$F_f = \begin{cases} \text{sat}\left(F_a, F_c\right), & \text{when } v_r = 0 \\ \left[F_c + (F_s - F_c)\, e^{-(v_r / v_s)^2} \right] \text{sgn}(v_r), & \text{else} \end{cases} \tag{5.28}$$

The shear ram block friction parameters used in the simulations are presented in Table 5.4. The level of uncertainty of the information available regarding these parameters

is high. For any specific application, the ideal method of identifying parameters are by experimental validation. The parameters used in this study are based on a lubricated steel-on-steel contact surface, adapted from [51], and should be considered as assumptions.

Mass of ram block	m_r	1718 kg
Gravity	g	9.81 m/s^2
Kinetic friction coefficient	μ_c	0.11
Static friction coefficient	μ_s	0.16
Stribeck characteristic velocity	v_s	0.001 m/s

Table 5.4: Friction parameters used in simulations.

The friction model is implemented in the Simulink model by using standard Simulink blocks. Figures of the friction model are included in Appendix B Figures B.5-B.7.

5.4.2 Wellbore Pressure

A simplified representation of the opposing force created by the wellbore pressure can be derived based on the basic equation describing hydrostatic force, given by,

$$F_p = \frac{\rho_m g h_m A_r}{2} \tag{5.29}$$

where F_p is the opposing force exerted on the ram block, ρ_m is the drilling mud density, A_r is the area of the shear ram block assembly on which the pressure is exerted on, and h_m is the height of the drilling mud column. The division factor of 2 is included due to the model restrictions previously mentioned.

The parameters used in the simulations are presented in Table 5.5, and are based on an arbitrary well. The pressure area of the ram block assembly A_r is assumed to be straight and rectangular, with dimensions adapted from the GateRam™ design presented in Section 4.2.

The height of the drilling mud column is the total length from the drilling rig to the BOP located at the seabed. Obviously, this depends on the water depth of the specific well, which varies widely. This is also the case for the drilling mud density, which depends

on the formation pressures present in the specific well. However, most wells are drilled with mud densities between 0.9-2.5 g/cm^3 [52].

Shear ram block width	w_r	47.7 cm (18.78 in)
Shear ram block height	h_r	12.7 cm (5 in)
Shear ram block pressure area	A_r	606 cm^2
Drilling mud density	ρ_m	1.5 g/cm^3
Drilling mud column height	h_m	2000 m

Table 5.5: Wellbore parameters used in simulations.

The wellbore pressure force is implemented in the Simulink model by using standard Simulink blocks.

5.5 Actuator Faults

This section introduces the modeling of the electro-mechanical shear ram actuator faults presented in Section 4.4. The faults are implemented directly in the model, or by modeling expected system behavior for the respective faults.

5.5.1 Planetary Gear Faults

Two planetary gear faults are considered - sun gear tooth cracks and general gear wear.

Sun Gear Tooth Crack

A gear tooth crack or spall defect can be described as a momentary loss off contact between two teeth in mesh, leading to a corresponding loss in gear mesh stiffness when the faulty tooth passes through the gear mesh [53]. The time-varying gear mesh stiffness function for a healthy and faulty tooth is illustrated in Figure 5.9.

The length and width of a crack or spall defect affect the loss of mesh stiffness, and it has been shown in research that the mesh stiffness is reduced proportionally to the damage severity [53, 54]. The assumed stiffness loss for tooth damages of varying degrees are given in Table 5.6, and are based on a study carried out by Zhang et.al. [37].

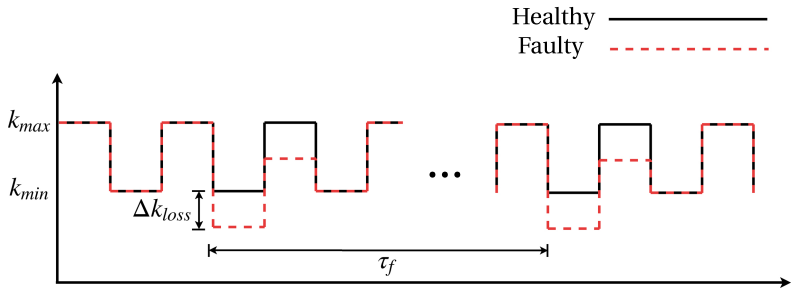

Figure 5.9: Time-varying gear mesh stiffness function of a healthy (solid black) and a faulty (dotted red) tooth. k_{max} is the maximum mesh stiffness, k_{min} is the minimum mesh stiffness, and Δk_{loss} is the mesh stiffness loss due to tooth crack. τ_f is the damaged gear tooth meshing period.

Slight fault	$\Delta k_{loss} = 0.4 \cdot 10^8$ Nm/rad
Moderate fault	$\Delta k_{loss} = 0.8 \cdot 10^8$ Nm/rad
Severe fault	$\Delta k_{loss} = 1.2 \cdot 10^8$ Nm/rad

Table 5.6: Gear tooth mesh stiffness loss due to tooth damage.

In this study, a crack is introduced at one of the sun gear teeth in the planetary gear. The crack is implemented in the model by extending the time-varying mesh stiffness function for a healthy tooth mesh presented in equation (5.19) so that it matches the faulty waveform illustrated in Figure 5.9. Because the faulty tooth is located on the sun gear, the sun-planet gear mesh stiffness function is extended. This is done by subtracting the healthy tooth contact square waveform Fourier series by a square waveform Fourier series with frequency equal to the mesh frequency of the faulty tooth. Thus, the mesh stiffness between the ith planet gear and a faulty sun gear can be described by,

$$K_{sp_i,f}(t) = K_{sp_i}(t) - \sum_{n=1}^{\infty} a_{n,f} cos\left(n\omega_s t - 2\pi n\left(\frac{i}{p} + \frac{1}{N_s p}\right)\right) \tag{5.30}$$

$$a_{n,f} = \sum_{n=1}^{\infty} \frac{2\Delta k_{loss}}{n\pi} sin\left(\frac{n\pi}{N_s}\right) \tag{5.31}$$

where $K_{sp_i}(t)$ is the time-varying mesh stiffness function for a healthy tooth mesh, ω_s is the angular velocity of the sun gear, i is the planet gear number, N_p is the total number of planet gears, and N_s is the number of sun gear teeth.

The tooth cracks introduce a fault frequency in the system based on the frequency at which the fault occurs. As the faulty tooth is in mesh N_p times for every revolution of the sun gear, the expected fault frequency $f_{f,pg}$ is described by,

$$f_{f,pg} = \frac{\omega_s}{2\pi} N_p \tag{5.32}$$

The instantaneous reduction in gear mesh stiffness will induce mechanical torsional vibrations in the system, which in electromechanical drives are known to affect the stator current [55]. The link between the torsional vibrations and stator current is somewhat complex, as it is in fact a result of the torsional vibrations superimposed on the rotor angular velocity, causing perturbations of the electromagnetic flux in the machine. As stated in Section 4.4, previous research has successfully detected planetary gear fault frequencies in the stator current as a sideband of the gear mesh frequency f_m [16, 37, 38], for both sun gear and ring gear faults. It should be noted, however, that the related research found concerns a damaged planetary gear in which the output shaft is connected to and drives a permanent magnet synchronous generator.

Gear Wear

In general, surface fatigue faults, i.e. localized or distributed faults, will modify the gear mesh stiffness. If the contact region between two teeth is completely contained in the surface fault, tooth contact is lost and stiffness will reduce gradually [56]. As the gear teeth wear and the surface hardness decreases, the contact zone increases, and the mesh stiffness decreases. Thus, to implement gear wear in the model, a uniform reduction of gear mesh stiffness is introduced, where the reduction is given as a percentage of wear. The reduced gear tooth mesh stiffnesses used in simulations are given in Table 5.7.

20% wear	$k_{max} = 4 \cdot 10^8$ Nm/rad	$k_{min} = 2.4 \cdot 10^8$ Nm/rad
40% wear	$k_{max} = 3 \cdot 10^8$ Nm/rad	$k_{min} = 1.8 \cdot 10^8$ Nm/rad
60% wear	$k_{max} = 2 \cdot 10^8$ Nm/rad	$k_{min} = 1.2 \cdot 10^8$ Nm/rad
80% wear	$k_{max} = 1 \cdot 10^8$ Nm/rad	$k_{min} = 0.6 \cdot 10^8$ Nm/rad

Table 5.7: Gear tooth mesh stiffness loss due to wear.

As with the planetary gear tooth crack, stiffness reduction in the gear due to wear will increase mechanical torsional vibrations in the system, which can be seen in the torsional response of the gear. Further, increased wear is expected to lead to increased oscillations in the stator current.

5.5.2 Motor Bearing Fault

It is well known that motor bearing faults induces additional impulse forces to the rotor, which is characterized as torque pulsations. Additionally, a bearing fault causes radial movement of the rotor, hence, a variation in air-gap (i.e. the distance between the rotor and stator) is introduced [57]. As the torque oscillations are introduced at specific frequencies and influences the stator current, it is possible to detect and diagnose a motor bearing fault by use of MCSA.

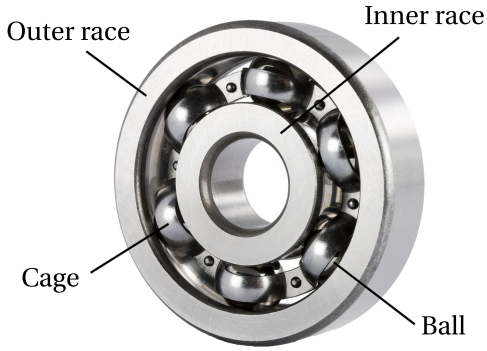

Figure 5.10: Ball bearing. Adapted from [58].

In general, a rolling-element bearing consists of two bearing rings (outer and inner raceways) and rolling elements (balls or rollers). The rolling elements are placed in cages that reduce friction. A ball bearing is illustrated in Figure 5.10. Local bearing damages can be classified in outer race faults, inner race faults, and roller faults. The various faults can be modeled by means of characteristic fault frequencies of the mechanical vibrations present due to the fault. The characteristic fault frequencies for the various faults can be described by,

$$f_{outer} = \frac{N_b}{2} f_{rm} \left(1 - \frac{d_b}{d_c} cos\beta\right) \tag{5.33a}$$

$$f_{inner} = \frac{N_b}{2} f_{rm} \left(1 + \frac{d_b}{d_c} cos\beta\right) \tag{5.33b}$$

$$f_{ball} = \frac{d_b}{d_c} f_{rm} \left(1 - \left(\frac{d_b}{d_c} cos\beta\right)^2\right) \tag{5.33c}$$

where f_{outer}, f_{inner} and f_{ball} are the fault frequencies for outer race, inner race, and ball faults, respectively, f_{rm} is the mechanical rotational frequency of the rotor, N_b is the number of rolling elements, d_b is the rolling element diameter, d_c is the cage diameter, and β is the rolling element contact angle [57]. In this study, a ball bearing is assumed to guide and support the PMSM shaft. Further, an outer race fault is investigated. However, the following approach is not restricted to this type of fault and can be applied to the other fault types.

Every time a ball passes through the damage point in the outer race, a torque disturbance will occur. Thus, the frequency of the disturbance is f_{outer}. The disturbance can be modeled as a square waveform pulse, whose width is dependent on the width of the damage, and whose amplitude is dependent on the weighting of the damage [59]. The square waveform can be represented as a Fourier series as,

$$T_{bf}(t) = A_{bf} \sum_{n=1}^{\infty} a_{n,bf} cos\left(nt \frac{1}{P_f}\right) \tag{5.34a}$$

$$a_{n,bf} = \sum_{n=1}^{\infty} \frac{2}{n\pi} sin\left(n\pi \frac{\Delta_f}{P_f}\right) \tag{5.34b}$$

where A_{bf} is the amplitude of the torque disturbance related to the bearing damage, described by,

$$A_{bf} = \alpha_f T_{load}, \qquad \alpha_f \in [0,1] \tag{5.35}$$

where α_f is the weighting of the damage related to the load torque.

Δ_f is the time of the high state of the square waveform, i.e. the time in which a ball passes through the damage, which is given as,

$$\Delta_f = \frac{d_f}{v_{To}} \tag{5.36a}$$

$$v_{To} = \frac{\omega_r}{2\left(1+\frac{d_b}{d_i}\right)} r_{rg} \tag{5.36b}$$

where d_f is the width of the damage, v_{To} is the outer race tangential velocity, d_i is the diameter of the inner race, and r_{rg} is the raceway groove radius [60].

P_f is the period of the square waveform, and is given as,

$$P_f = \frac{f_{rm}}{\omega_r f_{outer}} \tag{5.37}$$

The torque of the PMSM given in equations (5.6) through (5.10), can be expressed as the sum of the load torque T_{load} and the moment of inertia J_m,

$$T_e(t) = T_{load}(t) + J \cdot \frac{d}{dt}\omega_r(t) \tag{5.38}$$

Equation (5.38) is modified to include the torque disturbance, so that the torque is described by,

$$T_e(t) = T_{load}(t) + J \cdot \frac{d}{dt}\omega_r(t) + T_{bf}(t) \tag{5.39}$$

This torque disturbance is expected to induce oscillations in the stator current with the frequency $f_{f,bf}$,

$$f_{f,bf} = f_e \pm k \cdot f_{outer}, \qquad k = 1,2,3,\ldots \tag{5.40}$$

where f_e is the electrical supply frequency.

The torque disturbance is implemented in the Simulink model by modifying the torque equation of the custom PMSM Simscape block. The Simscape code is included in Appendix A Listings A.1-A.2. The bearing parameters used in the simulations are given in Table 5.8.

Inner race diameter	d_i	30 mm
Outer race diameter	d_o	70 mm
Ball diameter	d_b	11.5 mm
Cage diameter	d_c	50.5 mm
Raceway groove radius	r_{rg}	31.1 mm
Number of balls	N_b	11
Rolling element contact angle	β	0 deg

Table 5.8: Bearing parameters used in simulations.

5.5.3 Increased Shear Ram Block Friction

Increased shear ram block friction is introduced in the electro-mechanical shear ram actuator model by increasing the static and kinetic friction coefficients of the ram block, as presented in Section 5.4.1. The increased friction coefficients used in simulations are given in Table 5.9.

20% friction increase	$\mu_c = 0.13$	$\mu_s = 0.19$
50% friction increase	$\mu_c = 0.17$	$\mu_s = 0.24$
100% friction increase	$\mu_c = 0.22$	$\mu_s = 0.32$
200% friction increase	$\mu_c = 0.33$	$\mu_s = 0.48$
500% friction increase	$\mu_c = 0.66$	$\mu_s = 0.96$
1000% friction increase	$\mu_c = 1.21$	$\mu_s = 1.76$
1500% friction increase	$\mu_c = 1.76$	$\mu_s = 2.56$
2000% friction increase	$\mu_c = 2.31$	$\mu_s = 3.36$

Table 5.9: Ram block friction parameters used in simulations.

As the friction increases, more motor torque is required to counteract the opposing friction force and initialize motion of the ram block. Hence, the motor is expected to consume more power and draw more current.

Chapter 6

Fault Detection

This chapter will introduce the techniques that are used to extract fault signatures from simulation data obtained from simulations of the electro-mechanical shear ram actuator model. The techniques used include time domain analysis and spectral (frequency domain) analysis.

6.1 Time Domain Analysis

Of the key condition indicators used in this study, the root mean square (RMS), peak-to-peak, and crest factor (CF) values of the time domain signals have been chosen, because a change in their values can be a leading indicator of impending faults. Further, all three are common parameters used in conjunction with condition monitoring.

6.1.1 Root Mean Square

The RMS of a signal is defined as the square root of the mean square. For a set of n values, the RMS is described by,

$$x_{rms} = \sqrt{\frac{1}{n} x_1^2 + x_2^2 + \cdots + x_n^2} \tag{6.1}$$

It is commonly used in condition monitoring for detecting an overall increase of a signal. In vibration monitoring, RMS values have been used to detect the overall vibration level of gearboxes. The limitation of RMS is that it does not increase with isolated signal peaks. Hence, it is not sensitive to faults that only induces specific fault frequencies in a signal [61].

RMS values of measurement signals is obtained by using the Matlab function `rms`.

6.1.2 Peak-to-Peak

The peak-to-peak amplitude of a signal is the difference between peak, the highest amplitude value, and trough, the lowest amplitude value, which may be negative. Although this parameter can reveal system faults, it is usually not used alone.

Peak-to-peak values of measurement signals is obtained by using the Matlab function `peak2peak`.

6.1.3 Crest Factor

The CF is defined as the peak-to-peak value of the signal $x_{peak-to-peak}$ divided by the RMS value of the signal x_{rms},

$$CF = \frac{x_{peak-to-peak}}{x_{rms}} \tag{6.2}$$

The use of CF makes it possible to detect faults that lead to an increase in peak value, while the RMS value remains the same [61].

6.2 Spectral Analysis

The spectral analysis performed in this study is based on the Fast Fourier Transform (FFT) algorithm, which is perhaps the most common technique in spectral analysis of sensor signals. FFT makes it possible to detect the characteristic fault frequencies related to the specific faults, as discussed in Section 5.5.

6.2.1 Fast Fourier Transform

The FFT algorithm is an algorithm that rapidly computes the Discrete Fourier Transform (DFT) of a data sequence. The DFT has a forward and inverse form, described by,

$$X_k = \sum_{n=0}^{N-1} x_n e^{-\frac{2\pi i}{N} kn} \tag{6.3}$$

$$x_n = \frac{1}{N} \sum_{n=0}^{N-1} X_k e^{\frac{2\pi i}{N} kn} \tag{6.4}$$

where the transformation from x_n to X_k is a translation from configuration space to frequency space. The most common FFT algorithm is the Cooley-Turkey algorithm, where the general idea is to divide the DFT computation into smaller portions by using a divide-and-conquer approach, which in turn drastically decreases the computation time [62]. Thus, the most important difference from the conventional DFT computation method is that the FFT is much faster.

An important limitation of the FFT algorithm is that the frequency change within a single time interval is assumed small. Time information is lost in the transform, and it is impossible to tell when a particular event took place. When analyzing a stationary signal, e.g. sensor signals from a machine in steady state, this drawback is insignificant. However, the FFT algorithm is unable to detect periodic faults in the machine under non-stationary conditions that exist for a short period of time, e.g. during start-up, in which time-frequency approaches must be used.

The spectrum of a measurement signal is obtained by using the Matlab function `fft`. The code used for FFT plots is included in Appendix C Listing C.1.

Chapter 7

Simulation Results

In this chapter, the results from the simulations of the electro-mechanical shear ram model, and signal processing of simulation data are presented. The simulations represented the 10 first seconds of a shear ram function test, where the actuator was used to close the shear ram. The system was analyzed in its steady-state, i.e. after system transients had disappeared, by using measurements only from the 4 last seconds of each simulation.

A total of 21 simulations were executed for various system states, in which details are presented in Table 7.1. Further, Tables 4.1, 5.1-5.4 provides the parameters used for the simulation of the electro-mechanical shear ram actuator, while Tables 5.6-5.9 provides the parameters used to introduce the presented actuator faults in the model. The Simulink model diagram is included in Appendix B Figure B.8.

For the spectral analysis of the stator current, $dq0$-transformed current measurements were used in order to remove the fundamental electrical supply frequency f_e, which could otherwise mask the frequency sidebands arising from the faults introduced.

#	**System Condition**	**Parameters Affected**	**Value**
1	Healthy		
2	1st planetary gear sun gear tooth crack	Δk_{loss_1}	$0.4 \cdot 10^8$ Nm/rad
3	1st planetary gear sun gear tooth crack	Δk_{loss_1}	$0.8 \cdot 10^8$ Nm/rad
4	1st planetary gear sun gear tooth crack	Δk_{loss_1}	$1.2 \cdot 10^8$ Nm/rad
5	2nd planetary gear sun gear tooth crack	Δk_{loss_2}	$0.4 \cdot 10^8$ Nm/rad
6	2nd planetary gear sun gear tooth crack	Δk_{loss_2}	$0.8 \cdot 10^8$ Nm/rad
7	2nd planetary gear sun gear tooth crack	Δk_{loss_2}	$1.2 \cdot 10^8$ Nm/rad
8	Planetary gear wear	$k_{max_{1,2}}, k_{min_{1,2}}$	-20%
9	Planetary gear wear	$k_{max_{1,2}}, k_{min_{1,2}}$	-40%
10	Planetary gear wear	$k_{max_{1,2}}, k_{min_{1,2}}$	-60%
11	Planetary gear wear	$k_{max_{1,2}}, k_{min_{1,2}}$	-80%
12	Motor bearing fault	d_f	1 mm
13	Motor bearing fault	d_f	4 mm
14	Increased shear ram block friction	μ_s, μ_c	+20%
15	Increased shear ram block friction	μ_s, μ_c	+50%
16	Increased shear ram block friction	μ_s, μ_c	+100%
17	Increased shear ram block friction	μ_s, μ_c	+200%
18	Increased shear ram block friction	μ_s, μ_c	+500%
19	Increased shear ram block friction	μ_s, μ_c	+1000%
20	Increased shear ram block friction	μ_s, μ_c	+1500%
21	Increased shear ram block friction	μ_s, μ_c	+2000%

Table 7.1: Simulation details.

7.1 Healthy State

The electro-mechanical shear ram actuator model was simulated in its healthy state to provide a basis for comparison for the various actuator faults. Results from the healthy state simulation are provided for model verification purposes. The performance of the motor controller is shown in Figure 7.1, where rotor velocity ω_r and its reference ω_r^* are presented.

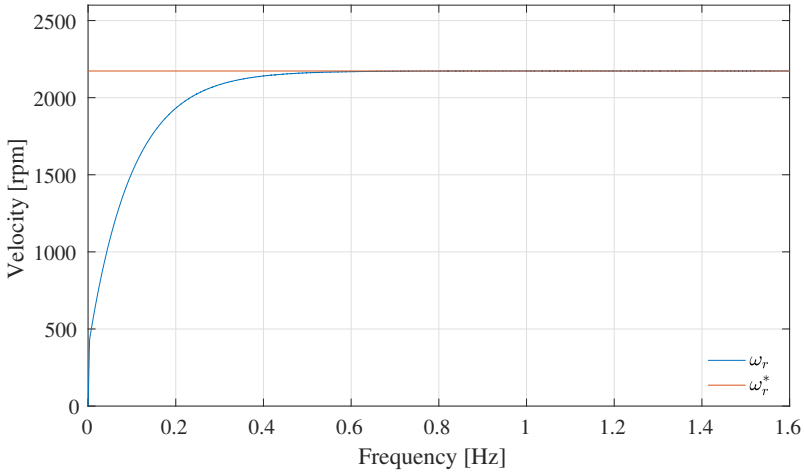

Figure 7.1: Rotor velocity ω_r and rotor reference velocity ω_r^* for healthy system.

The average velocities of the rotor, sun gear and carrier of the 1st planetary gear, carrier of the 2nd planetary gear and the shear ram block are presented in Table 7.2.

Component		**Average Velocity**
Rotor	ω_r	227.56 rad/s
1st planetary gear, sun gear	ω_{s_1}	84.91 rad/s
1st planetary gear, carrier	ω_{c_1}	8.99 rad/s
2nd planetary gear, carrier	ω_{c_2}	0.95 rad/s
Lead screw nut	v_n	3.8 mm/s

Table 7.2: Average mechanical velocities in steady-state.

Using the velocities presented in Table 7.2, the electrical supply frequency and gear

mesh frequencies apparent in the system were found. The frequencies are presented in Table 7.3.

Electrical supply frequency	f_e	144.87 Hz
1st planetary gear mesh frequency	f_{m_1}	283.79 Hz
2nd planetary gear mesh frequency	f_{m_2}	55.80 Hz

Table 7.3: Fundamental frequencies of the system in steady-state.

The a-phase current spectrum is presented in Figure 7.2, and clearly shows the fundamental electrical frequency of the current f_e.

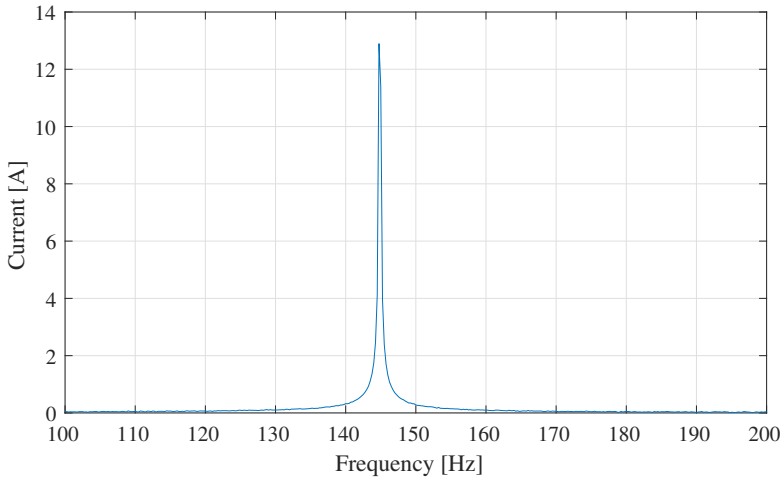

Figure 7.2: a-phase stator current spectrum for healthy system.

The q-axis current spectrum is presented in Figure 7.3. Two distinct frequencies are observed, which corresponds to the second harmonic of the 2nd planetary gear mesh frequency $2 \cdot f_{m_2}$, and the fundamental frequency of the 1st planetary gear mesh f_{m_1}.

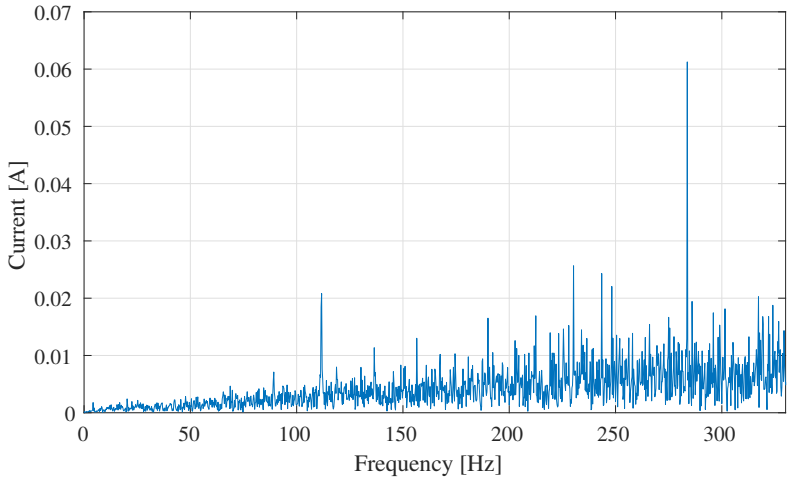

Figure 7.3: q-axis stator current spectrum for healthy system.

The applied force from the actuator F_a and the opposing forces F_p, F_f acting on the shear ram block in steady-state is presented in Table 7.4.

Applied force	F_a	714.8 kN
Wellbore pressure force	F_p	713.4 kN
Friction force	F_f	1391 N

Table 7.4: Forces acting on the shear ram block in steady-state.

7.2 Planetary Gear Faults

This section presents the results obtained after simulating faults in the planetary gears, where tooth cracks and gear wear was introduced.

7.2.1 Sun Gear Tooth Crack

A tooth crack was first introduced at the sun gear of the 1st planetary gear, then at the sun gear of the 2nd planetary gear. The opposing planetary gear was assumed healthy in both cases. Simulations were executed with cracks of varying severity. The expected

fault frequencies of the gear tooth cracks were obtained by using equation (5.32) and the steady-state velocities presented in Section 7.1, and are presented in Table 7.5.

1st planetary gear, sun gear tooth fault frequency	f_{f,pg_1}	40.54 Hz
2nd planetary gear, sun gear tooth fault frequency	f_{f,pg_2}	4.29 Hz

Table 7.5: Fault frequencies of the planetary gear tooth cracks.

To emphasize the difference between healthy and faulty state, the figures presented in this section are mainly based on results obtained with the most severe fault, where $\Delta k_{loss} = 1.2 \cdot 10^8$ Nm/rad.

1st Planetary Gear

The d-axis current spectrum for sun gear tooth crack in the 1st planetary gear is presented in Figure 7.4. Although the magnitude of some frequencies are larger in faulty state, including the second harmonic of the 2nd planetary gear mesh frequency $2 \cdot f_{m_2}$, no distinct frequencies related to the 1st planetary gear fault frequency f_{f,pg_1} were observed in this spectrum.

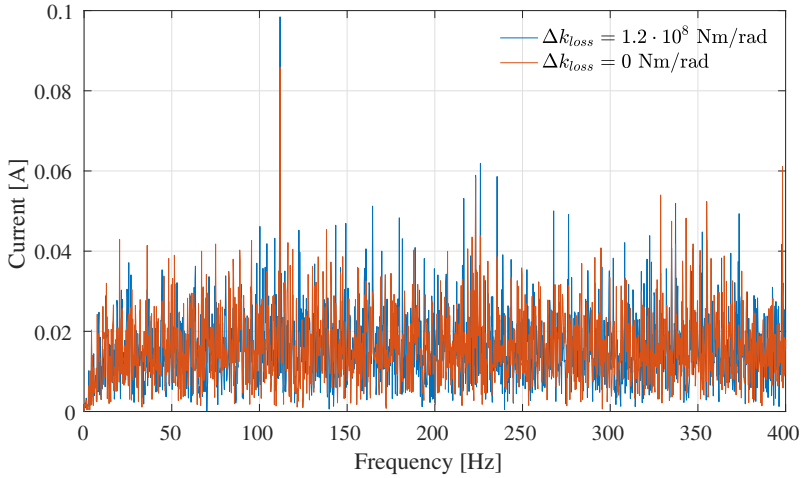

Figure 7.4: d-axis stator current spectrum, for healthy and damaged sun gear in the 1st planetary gear.

The q-axis current spectrum is presented in Figure 7.5. As in the d-axis spectrum, no distinct fault frequencies were observed. However, an increase in magnitude of the 1st planetary gear mesh frequency f_{m_1} was observed.

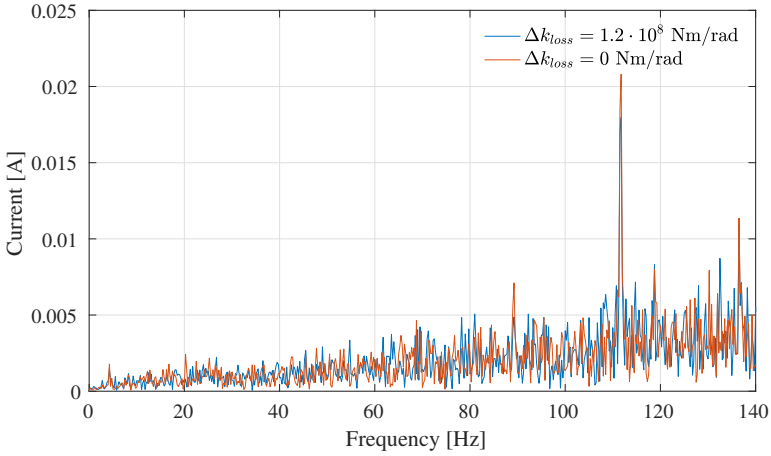

(a) Low frequency region

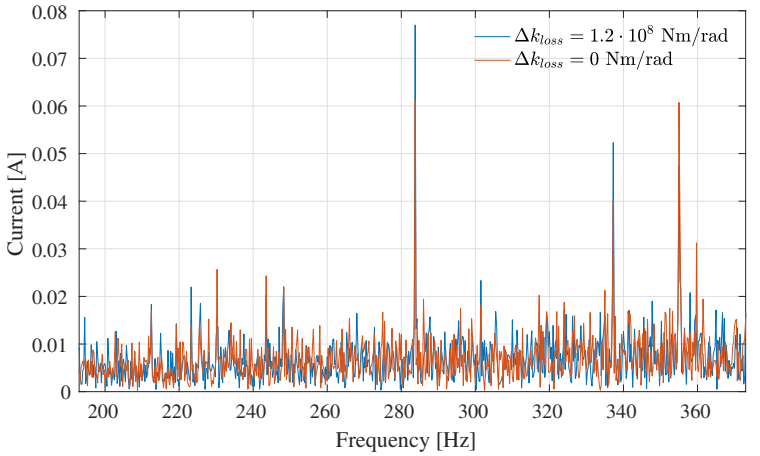

(b) f_{m_1} region

Figure 7.5: q-axis stator current spectrum, for healthy and damaged sun gear in the 1st planetary gear.

The spectrum of the 1st planetary gear carrier velocity ω_{c_1} is presented in Figure 7.6a. Several sidebands around the mesh frequency f_{m_1} were observed, located at $f_{m_1} \pm k \cdot f_{f,pg_1}$, or its equivalent $k \cdot f_{f,pg_1}$. Figure 7.6b shows how the magnitude of the frequency located at $f_{m_1} - 3 \cdot f_{f,pg_1}$ varied with fault severity. The sideband frequencies are presented in Table 7.6.

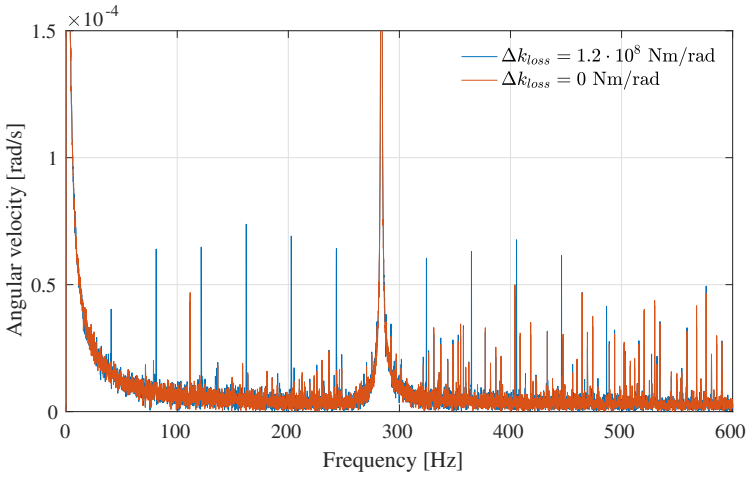

(a) f_{m_1} region

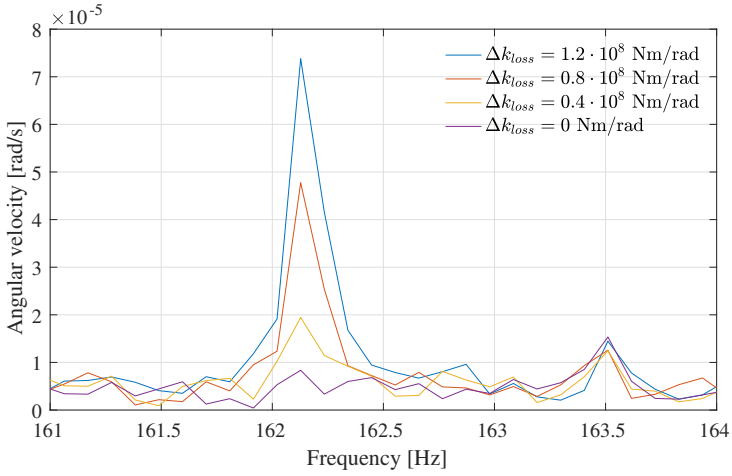

(b) $f_{m_1} - 3 \cdot f_{f,pg_1}$ region

Figure 7.6: 1st planetary gear carrier velocity $\omega_{c,1}$ spectrum, for healthy and damaged sun gear in the 1st planetary gear.

$f_{m_1} - 6 \cdot f_{f,pg_1}$	f_{f,pg_1}	40.54 Hz
$f_{m_1} - 5 \cdot f_{f,pg_1}$	$2 \cdot f_{f,pg_1}$	81.07 Hz
$f_{m_1} - 4 \cdot f_{f,pg_1}$	$3 \cdot f_{f,pg_1}$	121.60 Hz
$f_{m_1} - 3 \cdot f_{f,pg_1}$	$4 \cdot f_{f,pg_1}$	162.13 Hz
$f_{m_1} - 2 \cdot f_{f,pg_1}$	$5 \cdot f_{f,pg_1}$	202.66 Hz
$f_{m_1} - 1 \cdot f_{f,pg_1}$	$6 \cdot f_{f,pg_1}$	243.29 Hz
f_{m_1}	$7 \cdot f_{f,pg_1}$	283.79 Hz
$f_{m_1} + 1 \cdot f_{f,pg_1}$	$8 \cdot f_{f,pg_1}$	327.37 Hz
$f_{m_1} + 2 \cdot f_{f,pg_1}$	$9 \cdot f_{f,pg_1}$	364.89 Hz
$f_{m_1} + 3 \cdot f_{f,pg_1}$	$10 \cdot f_{f,pg_1}$	405.43 Hz
$f_{m_1} + 4 \cdot f_{f,pg_1}$	$11 \cdot f_{f,pg_1}$	445.96 Hz
$f_{m_1} + 5 \cdot f_{f,pg_1}$	$12 \cdot f_{f,pg_1}$	486.49 Hz
$f_{m_1} + 6 \cdot f_{f,pg_1}$	$13 \cdot f_{f,pg_1}$	527.03 Hz

Table 7.6: Characteristic fault frequencies for sun gear tooth crack on the 1st planetary gear.

The 1st planetary gear sun gear angular velocity ω_{s_1} spectrum is presented in Figure 7.7. The fault frequencies prominent in Figure 7.6 are not observed here.

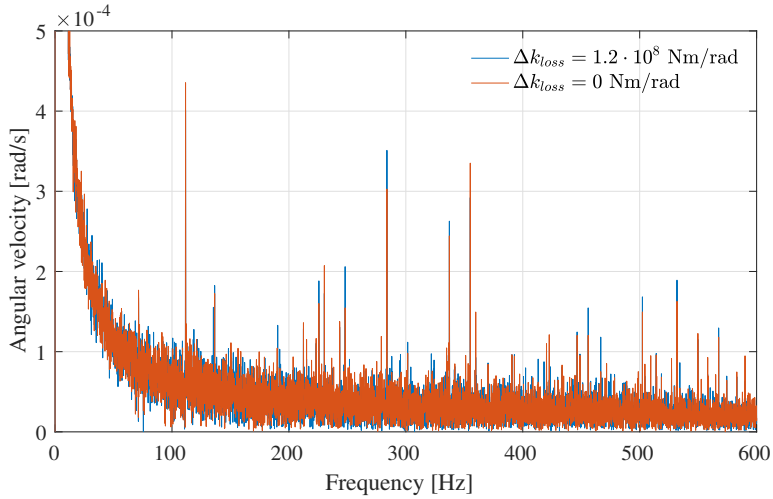

Figure 7.7: 1st planetary gear sun gear velocity ω_{s_1} spectrum, for healthy and damaged sun gear in the 1st planetary gear.

Figure 7.8 presents the 2nd planetary gear carrier velocity ω_{c_2} spectrum, with logarithmic y-axis. f_{m_2} was clearly dominant in this spectrum, but the fault frequencies located at $k \cdot f_{f,pg_1}$ were also observed.

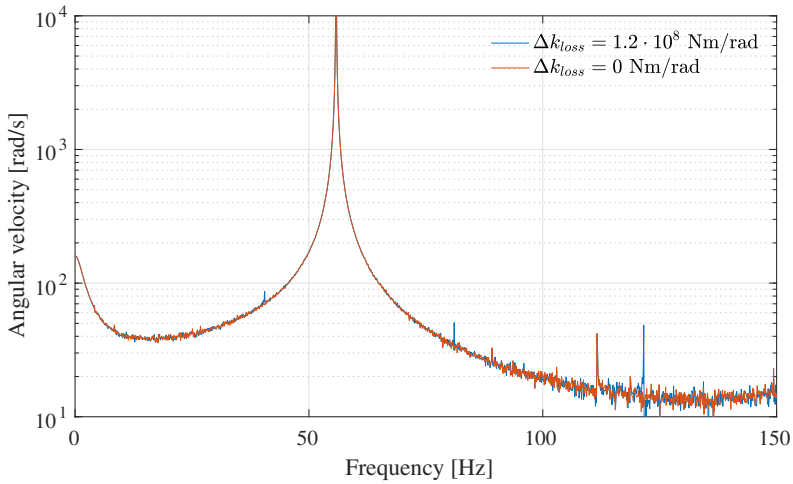

Figure 7.8: 2nd planetary gear carrier velocity ω_{c_2} spectrum with logarithmic y-axis, for healthy and damaged sun gear in the 1st planetary gear.

2nd Planetary Gear

The d- and q-axis current spectra for sun gear tooth crack in the 2nd planetary gear are presented in Figure 7.9 and 7.10, respectively. As with the sun gear tooth crack in the 1st planetary gear, no distinct frequencies related to the fault frequency f_{f,pg_2} were observed.

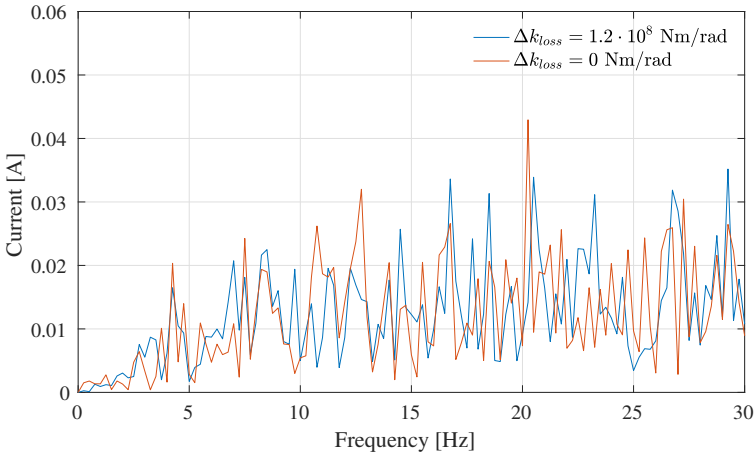

(a) Low frequency region

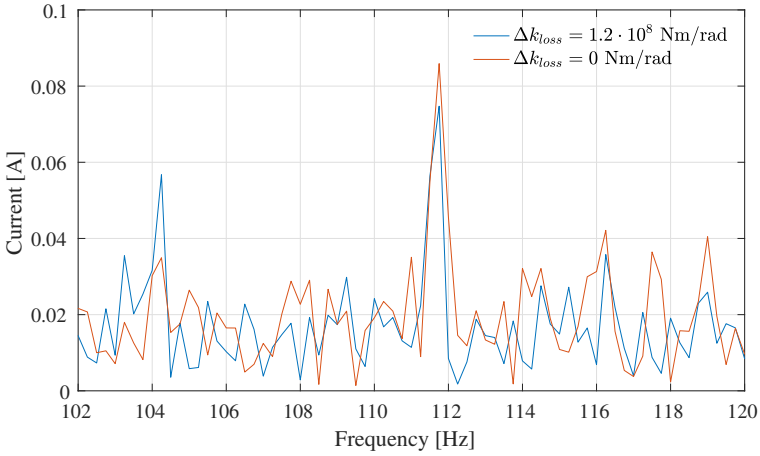

(b) f_{m_2} region

Figure 7.9: The d-axis stator current spectrum for healthy gear and damaged sun gear tooth on the 2nd planetary gear.

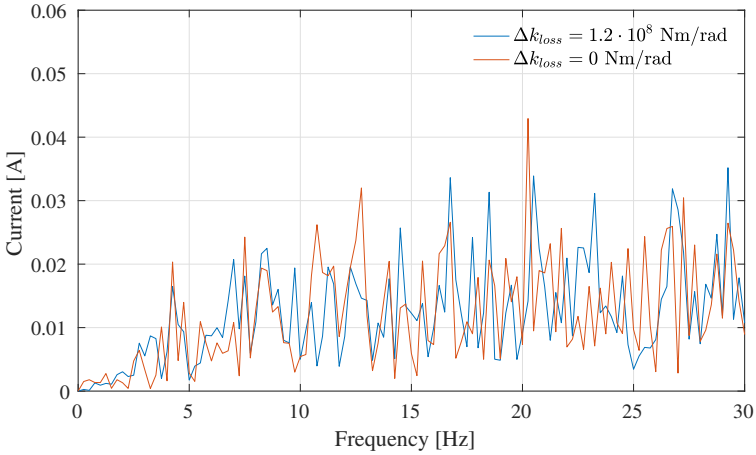

(a) Low frequency region

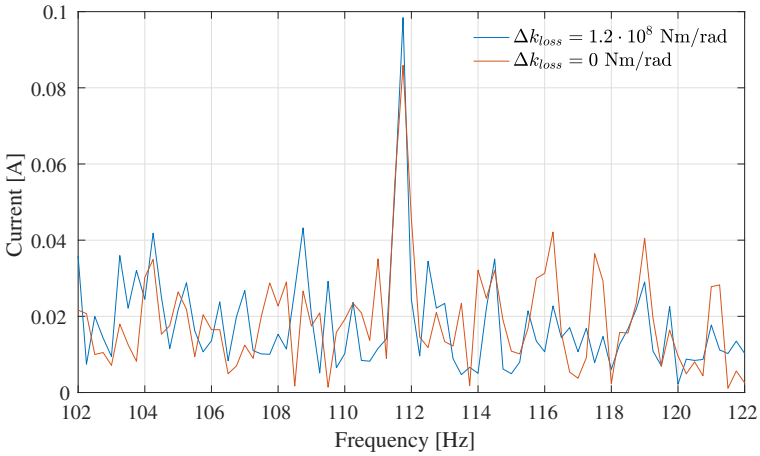

(b) $2 \cdot f_{m_2}$ region

Figure 7.10: The q-axis stator current spectrum for healthy gear and damaged sun gear tooth on the 2nd planetary gear.

The frequency spectrum of the 2nd planetary gear carrier velocity ω_{c_2} is presented in Figure 7.11a. Several sidebands around the mesh frequency f_{m_2} were observed, located at $f_{m_2} \pm k \cdot f_{f,pg_2}$, or its equivalent $k \cdot f_{f,pg_2}$. Figure 7.11b shows how the magnitude of the frequencies located at $f_{m_2} - 3 \cdot f_{f,pg_2}$ and $f_{m_2} - 4 \cdot f_{f,pg_2}$ varied with fault severity. Table 7.7 summarizes the characteristic frequencies present.

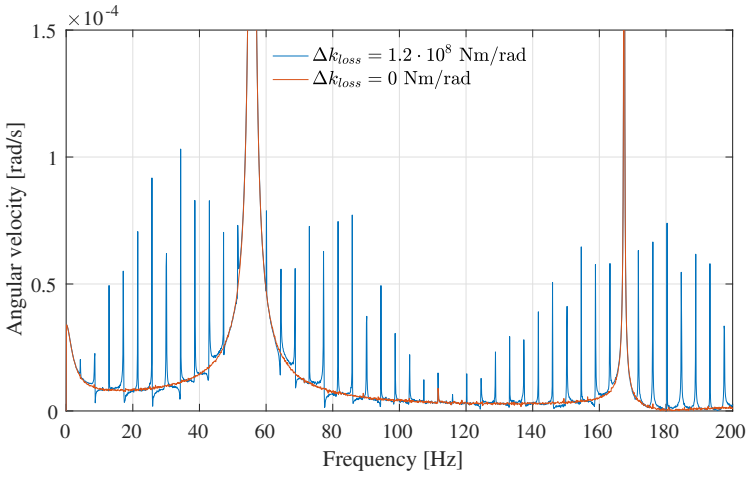

(a) f_{m_2} and $2 \cdot f_{m_2}$ region

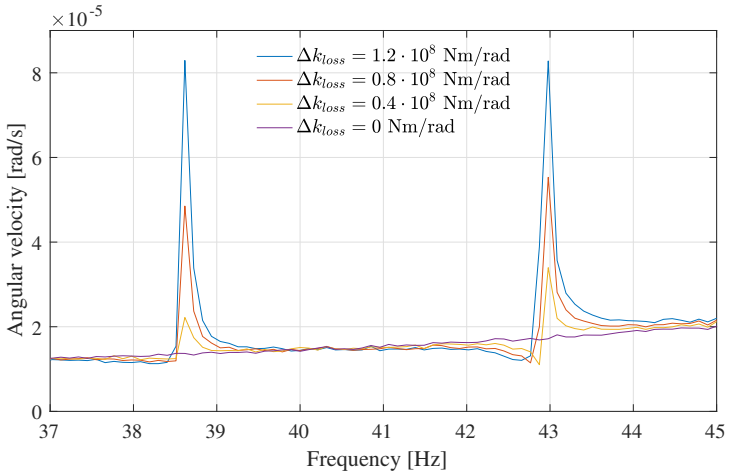

(b) $f_{m_2} - 3 \cdot f_{f,pg_2}$ and $f_{m_2} - 4 \cdot f_{f,pg_2}$ region

Figure 7.11: The 2nd planetary gear carrier velocity ω_{c_2} spectrum, for healthy gear and damaged sun gear tooth on the 2nd planetary gear.

$f_{m_2} - 12 \cdot f_{f,pg_2}$	f_{f,pg_2}	4.26 Hz
$f_{m_2} - 11 \cdot f_{f,pg_2}$	$2 \cdot f_{f,pg_2}$	8.62 Hz
$f_{m_2} - 10 \cdot f_{f,pg_2}$	$3 \cdot f_{f,pg_2}$	12.87 Hz
	$\vdots$	
$f_{m_2} - 6 \cdot f_{f,pg_2}$	$7 \cdot f_{f,pg_2}$	30.11 Hz
$f_{m_2} - 5 \cdot f_{f,pg_2}$	$8 \cdot f_{f,pg_2}$	34.37 Hz
$f_{m_2} - 4 \cdot f_{f,pg_2}$	$9 \cdot f_{f,pg_2}$	38.62 Hz
$f_{m_2} - 3 \cdot f_{f,pg_2}$	$10 \cdot f_{f,pg_2}$	42.98 Hz
$f_{m_2} - 2 \cdot f_{f,pg_2}$	$11 \cdot f_{f,pg_2}$	47.24 Hz
$f_{m_2} - 1 \cdot f_{f,pg_2}$	$12 \cdot f_{f,pg_2}$	51.49 Hz
f_{m_2}	$13 \cdot f_{f,pg_2}$	55.80 Hz
$f_{m_2} + 1 \cdot f_{f,pg_2}$	$14 \cdot f_{f,pg_2}$	60.11 Hz
$f_{m_2} + 2 \cdot f_{f,pg_2}$	$15 \cdot f_{f,pg_2}$	64.47 Hz
$f_{m_2} + 3 \cdot f_{f,pg_2}$	$16 \cdot f_{f,pg_2}$	68.72 Hz
$f_{m_2} + 4 \cdot f_{f,pg_2}$	$17 \cdot f_{f,pg_2}$	72.98 Hz
$f_{m_2} + 5 \cdot f_{f,pg_2}$	$18 \cdot f_{f,pg_2}$	77.24 Hz
$f_{m_2} + 6 \cdot f_{f,pg_2}$	$19 \cdot f_{f,pg_2}$	81.60 Hz

Table 7.7: Characteristic fault frequencies for sun gear tooth crack on the 2nd planetary gear.

The 2nd planetary gear sun gear velocity spectrum is presented in Figure 7.12. As with the 1st planetary gear sun gear damage, the fault frequencies prominent at the carrier velocity spectrum are not observed here.

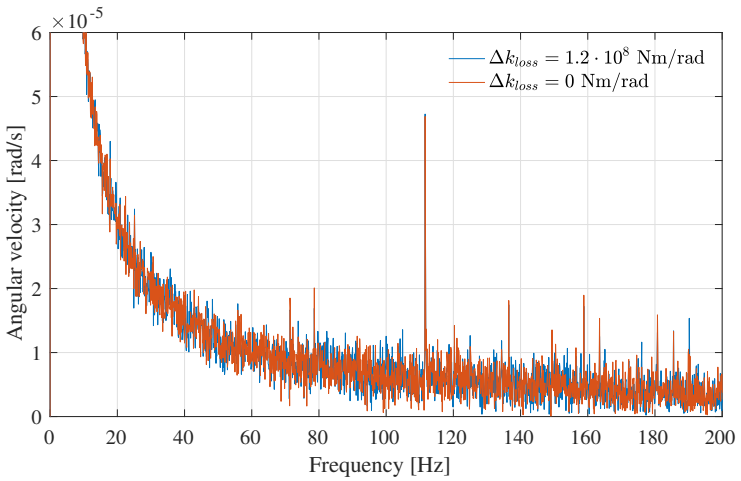

Figure 7.12: The 2nd planetary gear sun gear velocity ω_{s_2} spectrum, for healthy and damaged sun gear in the 2nd planetary gear.

7.2.2 Gear Wear

Planetary gear wear was implemented in the model by reducing the maximum and minimum value of gear mesh stiffness, k_{max} and k_{min}. Simulations were executed with the stiffnesses reduced by 20%, 40%, 60% and 80% of its original value. The mesh stiffness reduction was introduced at both planetary gears simultaneously.

The 2nd planetary gear carrier angular velocity ω_{c_2} for all cases are presented in Figure 7.13. The constant component was removed to accentuate the difference between the fault cases. It was observed that both the peak-to-peak and RMS values of the velocity signal increased with stiffness reduction, and accordingly the effects of wear. The CF values decreased with increased stiffness reduction. The peak-to-peak, RMS and CF ω_{c_2} values are presented in Table 7.8.

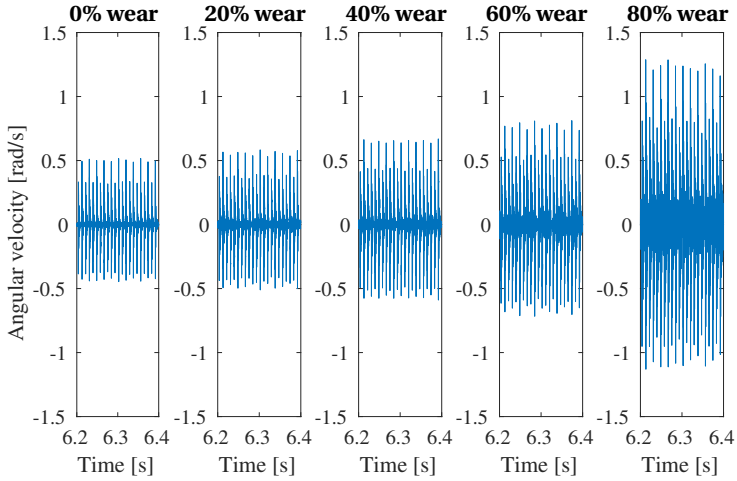

Figure 7.13: The 2nd planetary gear carrier velocity ω_{c_2} for all increased gear wear cases.

$\mathbf{k_{max}}$, $\mathbf{k_{min}}$	$\omega_{\mathbf{c_2}}$ **peak-to-peak**	$\omega_{\mathbf{c_2}}$ **RMS**	$\omega_{\mathbf{c_2}}$ **CF**
Healthy	0.98 rad/s	0.09 rad/s	10.91
-20 %	1.10 rad/s	0.11 rad/s	10.28
-40%	1.26 rad/s	0.13 rad/s	9.38
-60%	1.56 rad/s	0.18 rad/s	8.62
-80%	2.46 rad/s	0.34 rad/s	7.32

Table 7.8: Peak-to-peak, RMS, and CF values of the 2nd planetary gear carrier velocity ω_{c_2} for all increased gear wear cases.

The q-axis current for all gear wear cases are presented in Figure 7.14. As with the carrier velocities, the constant component was removed to accentuate the difference between the fault cases. It was observed that all of the peak-to-peak, RMS and CF values of the q-axis current increased with wear. The peak-to-peak, RMS and CF q-axis current values are presented in Table 7.9.

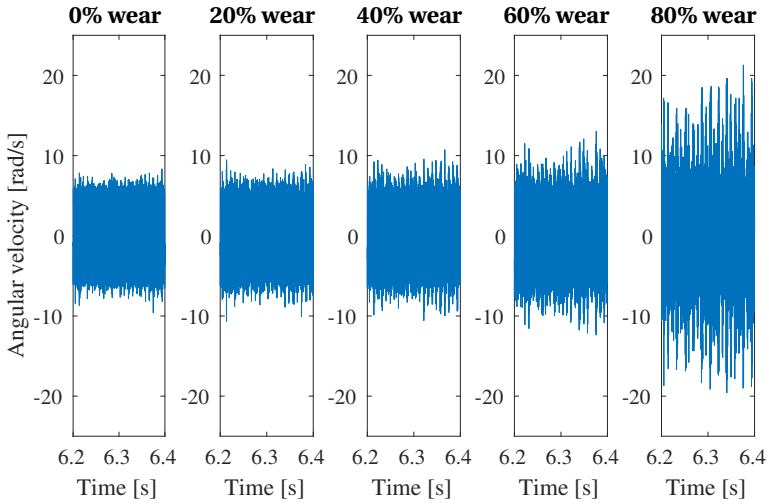

Figure 7.14: The q-axis stator current for all increased gear wear cases.

k_{max}, k_{min}	i_q peak-to-peak	i_q RMS	i_q CF
Healthy	18.60 A	3.34 A	5.57
-20 %	20.96 A	3.39 A	6.19
-40%	22.54 A	3.49 A	6.46
-60%	28.05 A	3.84 A	7.30
-80%	43.38 A	5.87 A	7.39

Table 7.9: Peak-to-peak, RMS, and CF values of the q-axis current for all increased gear wear cases.

The torsional vibrations induced by gear wear led to stator current oscillations at the mesh frequencies and sidebands located at $k \cdot f_m$, where $k = 1, 3, 5, \ldots$, as shown in Figure 7.15 where the q-axis current spectrum region around f_{m_2} is presented. In relation to the case of 0% wear, the introduction of gear wear was observed as a significant increase in the gear mesh frequencies magnitude, especially for the cases of 60% and 80% wear.

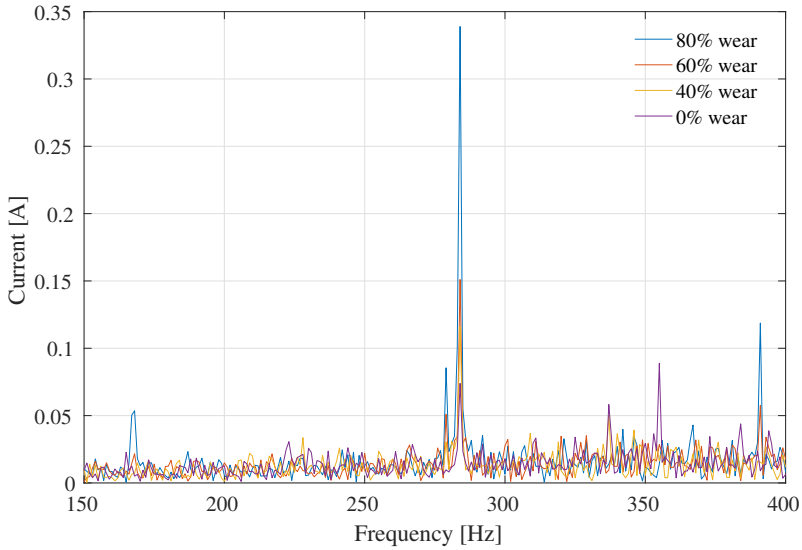

Figure 7.15: The q-axis stator current spectrum for increased gear wear.

7.3 Motor Bearing Fault

Motor bearing outer race faults were introduced with damage widths of 1 mm and 4 mm. The expected fundamental bearing fault frequency was found to be $f_{f,bf}$ = 153.5 Hz, by using the rotor velocity ω_r presented in Table 7.2 and the bearing parameters with equation (5.33a). The low frequency region of the q-axis current spectrum is presented in Figure 7.16a. A distinct peak at $f_{f,bf}$ was observed for both fault cases. A narrow view of the spectrum concentrated around $f_{f,bf}$ is presented in Figure 7.16b.

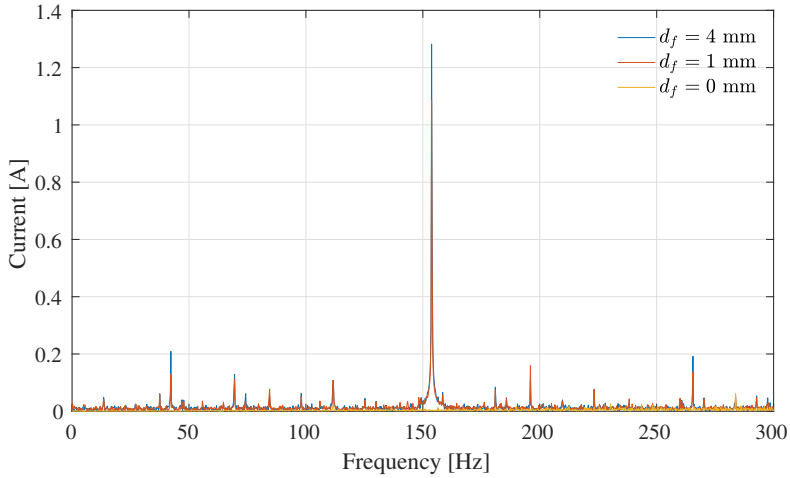

(a) Low frequency region

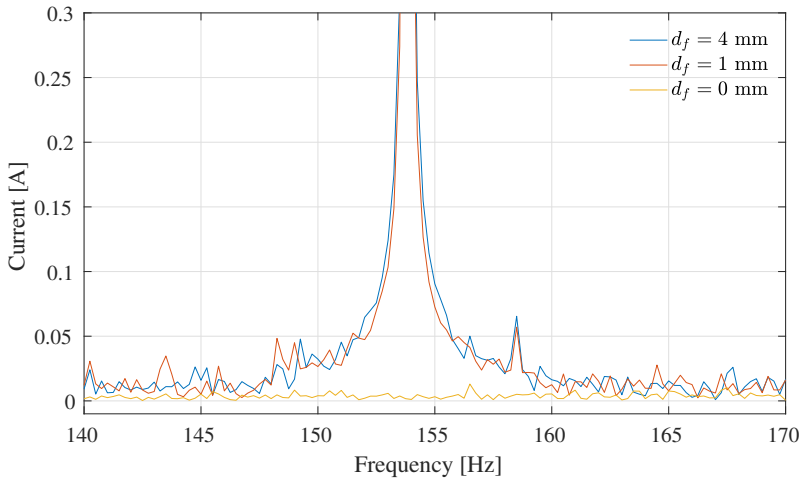

(b) $f_{f,bf}$ region

Figure 7.16: q-axis current spectrum for healthy bearing, 1 mm outer race damage and 4 mm outer race damage.

7.4 Increased Shear Ram Block Friction

Increased shear ram block friction was introduced in the model by increasing the friction coefficients μ_c and μ_c. The peak-to-peak, RMS and CF values of the a-phase current and q-axis current for all friction cases are presented in Table 7.10.

It was observed that both the a-phase and q-axis RMS currents increased as the friction increased. However, the peak-to-peak and CF values showed no clear relation to the friction increase.

μ_c, μ_s	i_a Peak-to-Peak	i_a RMS	i_a CF	i_q Peak-to-Peak	i_q RMS	i_q CF
Healthy	54.44 A	13.72 A	3.96	18.43 A	19.35 A	0.95
+20%	53.65 A	13.73 A	3.90	18.84 A	19.36 A	0.97
+50%	53.96 A	13.73 A	3.92	19.22 A	19.36 A	0.99
+100%	53.54 A	13.74 A	3.89	18.21 A	19.37 A	0.94
+200%	54.77 A	13.76 A	3.97	18.39 A	19.40 A	0.94
+500%	54.75 A	13.81 A	3.96	18.89 A	19.47 A	0.97
+1000%	55.03 A	13.90 A	3.95	18.73 A	19.59 A	0.95
+1500%	55.27 A	13.98 A	3.95	18.73 A	19.72 A	0.95
+2000%	55.56 A	14.06 A	3.95	18.70 A	19.84 A	0.94

Table 7.10: Peak-to-peak, RMS and CF values of a-phase and q-axis currents for all shear ram block friction cases.

Chapter 8

Discussion

This chapter provides a discussion of the results presented in Chapter 7.

8.1 Planetary Gear Tooth Cracks

In Figures 7.4-7.5 and 7.9-7.10, where the d- and q-axis current spectra for the sun gear tooth crack fault in the 1st and 2nd planetary gear are presented, no explicit fault frequencies are observed. As stated in Section 5.5.1, previous research has shown that a tooth fault is detectable by analyzing the stator current for fault frequencies. The main difference from this study and previous research is that the current analyzed is obtained from a machine driving a damaged planetary gear, whereas previous research concerns stator current analysis of a generator driven by a damaged gear. As is shown in Figures 7.6 and 7.11, where the velocity spectra of the carrier (or output shaft) of the damaged planetary gears are presented, the tooth fault induces periodic spikes in the output angular velocity. The spikes are present for all three fault cases, but are most evident for the moderate and severe faults. These spikes are torsional vibrations due to the mesh stiffness loss. However, as seen in Figures 7.7 and 7.12, the torsional vibrations does not affect the sun gear (or input shaft) velocity to the same extent. As it is seen from Figures 7.8 and 7.11, tooth cracks in both planetary gears are detected in the torsional

response of the 2nd planetary gear carrier. It is believed that this is the reason that the tooth cracks are not detected in the stator current spectra.

As presented in Section 3.5.4, a rotary encoder will be included in the actuator system for speed and position monitoring of the shaft that connects the planetary gears and the roller screw, i.e. the output shaft of the 2nd planetary gear. Based on these results, the rotary encoder may be used for detection of fault frequencies in the torsional vibrational response induced by planetary gear tooth cracks.

It should be noted that a simplified model of the spur gears is used, which does not consider mesh properties. However, as the spur gears are rotating at higher angular velocities, and have a higher number of teeth, the spur gear mesh frequencies are not likely to mask the mesh and fault frequencies of the planetary gears. Another limitation of the model used in this study is that the planetary gear model is purely torsional, meaning that no translational vibrational effects are considered. Although the tooth cracks are highly visible in the torsional response in this study, it may not be as easy to detect in practice. However, as the planetary gear output shafts are supported by bearings, it is sound to assume that the torsional vibrations will affect the translational vibration response of the bearings. Thus, accelerometers mounted on the bearings for translational vibrational monitoring may also be used for detection of fault frequencies induced by planetary gear tooth cracks.

8.2 Planetary Gear Wear

The limitations discussed in Section 8.1 must also be considered when studying the results obtained for the planetary gear wear faults, as presented in Figure 7.13 and Table 7.8. The results show that the torsional vibrations in the carrier/output shaft increase with the amount of wear, in which a significant increase is observed for the cases of 60% and 80% wear. All time-domain techniques used, i.e. RMS, peak-to-peak and CF, shows a clear connection to the amount of wear. As with the tooth faults, the torsional vibrations induced by increased wear are believed to affect the bearing vibrations, which are likely to be detectable by use of accelerometers, in addition to the rotary encoder.

Further, the torsional vibrations are reflected on to the stator current, as seen from the

data presented in Figure 7.14 and Table 7.9. As seen from Figure 7.15, the oscillations occurred at the mesh frequencies of the planetary gears. This is explained by the implementation of gear wear in the model, which is by reduction of the mesh stiffnesses that represents tooth contact at each gear mesh.

8.3 Motor Bearing Fault

As seen from Figure 7.16, the bearing fault frequency $f_{f,bf}$ is clearly visible in the stator current spectrum for both damage widths studied. The fault frequency is clearly distinguishable from the healthy state independent of the fault diameter d_f. However, the damage with a width of 4 mm has a slightly higher peak than the 1 mm wide damage, which makes sense as it is a more severe fault. The results obtained compares well to previous research, and show that stator current analysis is a potential method for motor bearing fault detection. Compared to traditional vibration monitoring, this is a cheaper and non-intrusive solution, as the current sensor will be implemented as part of the motor drive. Further, although only an outer race damage is studied, other types of bearing damages are expected to affect the system in a similar way, meaning that the same detection method will be applicable.

8.4 Increased Shear Ram Block Friction

The results presented in Table 7.10 shows a connection between the ram block friction and RMS current. However, the actual RMS current increase compared to the current consumed with normal shear ram block friction is small. This is explained by the relationship between the opposing friction force F_f, and the opposing force related to the wellbore pressure F_p. As presented in Section 7.1, F_p is significantly larger in magnitude compared to F_f. As the total force opposing the motion of the shear ram block is made up of both F_f and F_p, a large increase of F_f in terms of friction, may only be a small increase of the total opposing force. Hence, the relative increase in RMS current is small.

It should be noted that pressure compensation of the actuator is not considered in this

model, which can help lower the ratio between the two opposing forces, and emphasize the friction increase in the current response. However, varying wellbore pressure will complicate detection of increased shear ram block friction, as the opposing force will vary greatly. It is obvious that the use of current monitoring for detection of increased friction relies on a well-developed monitoring system that accounts for variation in accompanying external forces.

8.5 Future Work

Suggestions for further work regarding the actuator model can be to implement detailed models of the roller screw mechanism and spur gears. Translational effects of the planetary gear faults should be studied by extending the planetary gear model. Further, the model can be extended to consider both actuator transmissions. The same faults should be compared to an extended model to see if the results hold. At last, if feasible, the results should be proved by experimental validation of the model.

Further work regarding fault detection is to implement or develop algorithms that highlight a fault condition and outputs a condition indicator based on the input data. The fault indicators can be used as input for intelligent condition monitoring systems, which should be able to classify different types of faults, allowing for autonomous fault detection and diagnostics.

Bibliography

[1] MCS Kenny, "Assessment of BOP Stack Sequencing, Monitoring and Kick Detection Technology - Final Report 02 - BOP Monitoring and Acoustic Technology," Tech. Rep., 2013.

[2] D. Nærheim, "Condition Monitoring of an All-Electric Blowout Preventer - Pre-Project," Tech. Rep., 2017.

[3] M. Laurens and M. Kales, "Moving beyond real-time operations centres," in *Society of Petroleum Engineers - International Petroleum Technology Conference 2014, IPTC 2014: Unlocking Energy Through Innovation, Technology and Capability*, vol. 4, 2014, pp. 3099–3106.

[4] International Organization for Standardization, "Condition monitoring and diagnostics of machines - General guidelines," *ISO 17359:2011*, 2011.

[5] A. K. Jardine, D. Lin, and D. Banjevic, "A review on machinery diagnostics and prognostics implementing condition-based maintenance," pp. 1483–1510, 2006.

[6] W. Q. Meeker and L. A. Escobar, *Statistical methods for reliability data*. Wiley, 1998.

[7] International Organization for Standardization, "Condition monitoring and diagnostics of machines – Requirements for qualification and assessment of personnel – Part 4: Field lubricant analysis," *ISO 18436:2014*, 2014.

[8] IEEE Standards Association, "IEEE Standard for Artificial Intelligence Exchange and Service Tie to All Test Environments (AI-ESTATE)," *IEEE 1232-2010*, 2010.

[9] S. Hernæs and T. Aas, "An Alternative Approach to 50 Years Design Life," in *Offshore Technology Conference*. Offshore Technology Conference, may 2015.

[10] G. Gola and B. H. Nystad, "Prognostics and Health Management of Choke Valves Subject to Erosion: A Diagnostic-Prognostic Frame for Optimal Maintenance Scheduling," *Diagnostics and Prognostics of Engineering Systems: Methods and Techniques*, pp. 313–331, 2013.

[11] B. H. Nystad, G. Gola, J. E. Hulsund, and D. Roverso, "Technical condition assessment and remaining useful life estimation of choke valves subject to erosion," in *Annual Conference of the Prognostics and Health Management society*, 2010, pp. 1–9.

[12] C. Y. Serene and L. P. Chze, "Subsea Condition Monitoring: Does Effective Diagnosis Increase Availability?" *Journal of Petroleum Technology*, vol. 67, no. 12, pp. 52–55, dec 2015.

[13] M. S. Patil, J. Mathew, and P. K. RajendraKumar, "Bearing Signature Analysis as a Medium for Fault Detection: A Review," *Journal of Tribology*, vol. 130, no. 1, p. 014001, jan 2008.

[14] M. Valencia, "TI Hercules RM57: FFT Magnitude Scale." [Online]. Available: https://e2e.ti.com/group/launchyourdesign/m/boosterpackcontest/666273{#}

[15] S. Nandi, H. A. Toliyat, and X. Li, "Condition monitoring and fault diagnosis of electrical motors - A review," pp. 719–729, 2005.

[16] J. Zhang, J. S. Dhupia, and C. J. Gajanayake, "Stator current analysis from electrical machines using resonance residual technique to detect faults in planetary gearboxes," *IEEE Transactions on Industrial Electronics*, vol. 62, no. 9, pp. 5709–5721, 2015.

[17] B. et.al. Boashash, *Time Frequency Analysis*. Elsevier, 2003. [Online]. Available: http://linkinghub.elsevier.com/retrieve/pii/B9780080443355X50207

[18] Transocean, “Macondo Well Incident, Transocean Investigation Report Volume I,” Tech. Rep., 2011. [Online]. Available: http://www.iadc.org/wp-content/uploads/2016/04/TRANSOCEAN-Macondo-Well-Incident-Investigation-Repport-Volume-I.pdf

[19] Egmason, “Blowout Preventer.svg,” 2011. [Online]. Available: https://commons.wikimedia.org/wiki/File:Blowout{_}Preventer.svg

[20] S. P. Vigeant, “Deepwater Driven Advancements in Well Control Equipment and Systems,” in *IADC/SPE Drilling Conference*. Society of Petroleum Engineers, apr 1998.

[21] H. McCrae, *Marine riser systems and subsea blowout preventers*. University of Texas at Austin, 2003.

[22] Bureau of Safety and Environmental Enforcement, “Oil and Gas and Sulfur Operations in the Outer Continental Shelf—Blowout Preventer Systems and Well Control,” *30 CFR § 250*, 2016.

[23] ——, “Oil and Gas and Sulfur Operations in the Outer Continental Shelf-Blowout Preventer Systems and Well Control Revisions,” *83 Federal Register 22128*, pp. 22 128–22 162, 2018.

[24] Norsk Sokkels Konkurranseposisjon, “Well Integrity in Drilling and Well Operations,” *NORSOK D-010:2013*, 2013.

[25] The American Petroleum Institute, “Blowout Prevention Equipment Systems for Drilling Wells, Fourth Edition, Includes Addendum 1,” *API Std 53*, 2012.

[26] B. Cach, “Feasibility Report El-Mech Ram 800T,” Transtech A/S, Tech. Rep., 2017.

[27] R. Krishnan, *Permanent Magnet Synchronous and DC Brushless Machines*, 1st ed. CRC Press, 2010.

[28] J. F. Gieras, *Permanent Magnet Motor Technology: Design and Applications*, 2013, vol. 53.

[29] A. Al-Shyyab and A. Kahraman, “A non-linear dynamic model for planetary gear sets,” *Proceedings of the Institution of Mechanical Engineers, Part K: Journal of Multi-body Dynamics*, vol. 221, no. 4, pp. 567–576, 2007.

[30] Creative Motion Control, "Customization and Prototypes." [Online]. Available: http://www.creativemotioncontrol.com/home-copy/cmc-roller-screws/

[31] SKF Group, *Roller screws*, 2014. [Online]. Available: http://www.skf.com/binary/21-153959/14489-EN---Roller-screw-catalogue.pdf

[32] International Electrotechnical Commission, "Functional safety of electrical/electronic/programmable electronic safety-related systems," *IEC 61508*, 2010.

[33] M. Kenny, "Final Report 01 - BOP Stack Sequencing and Shear Ram Design," Tech. Rep., 2013.

[34] I. Yesilyurt, F. Gu, and A. D. Ball, "Gear tooth stiffness reduction measurement using modal analysis and its use in wear fault severity assessment of spur gears," *NDT and E International*, vol. 36, no. 5, pp. 357–372, 2003.

[35] D. Goyal, B. Pabla, and S. Dhami, "Condition Monitoring Parameters for Fault Diagnosis of Fixed Axis Gearbox: A Review," *Archives of Computational Methods in Engineering*, 2016.

[36] D. M. Blunt and J. A. Keller, "Detection of a fatigue crack in a UH-60A planet gear carrier using vibration analysis," *Mechanical Systems and Signal Processing*, vol. 20, no. 8, pp. 2095–2111, 2006.

[37] J. Zhang, L. Hong, and J. Singh Dhupia, "Gear Fault Detection in Planetary Gearbox Using Stator Current Measurement of AC Motors," in *Volume 1: Adaptive Control; Advanced Vehicle Propulsion Systems; Aerospace Systems; Autonomous Systems; Battery Modeling; Biochemical Systems; Control Over Networks; Control Systems Design; Cooperativ*, 2012, pp. 673–680. [Online]. Available: http://proceedings.asmedigitalcollection.asme.org/proceeding.aspx?doi=10.1115/DSCC2012-MOVIC2012-8609

[38] J. S. Dhupia, "A time-domain fault detection method based on an electrical machine stator current measurement for planetary gear-sets," *2013 IEEE/ASME International Conference on Advanced Intelligent Mechatronics*, pp. 1631–1636, 2013. [Online]. Available: http://www.scopus.com/inward/record.url?eid=2-s2.0-84883689029{&}partnerID=tZOtx3y1

[39] A. H. Bonnett and C. Yung, "Increased efficiency versus increased reliability," *IEEE Industry Applications Magazine*, vol. 14, no. 1, pp. 29–36, 2008.

[40] R. Krishnan, *Electric Motor Drives: Modeling, Analysis and Control*, 1st ed. Prentice Hall, 2001.

[41] W. Huang, Y. Zhang, X. Zhang, and G. Sun, "Accurate Torque Control of Interior Permanent Magnet Synchronous Machine," *Energy Conversion, IEEE Transactions on*, vol. 29, no. 1, pp. 29–37, 2014.

[42] L. Harnefors, *Control of Variable-Speed Drives*, 1st ed. Department of Electronics, Mälardalen University, 2002.

[43] The MathWorks Inc., "PWM Generator (Three-phase, Two-level)," 2018.

[44] O. Egeland and T. Gravdahl, *Modeling and Simulation for Automatic Control*, 2nd ed., 2003.

[45] A. Kahraman, "Planetary Gear Train Dynamics," *Journal of Mechanical Design*, vol. 116, no. 3, p. 713, 1994.

[46] J. Lin and R. G. Parker, "Planetary gear parametric instability caused by mesh stiffness variation," *Journal of Sound and Vibration*, vol. 249, no. 1, pp. 129–145, 2002.

[47] M. Inalpolat and A. Kahraman, "A dynamic model to predict modulation sidebands of a planetary gear set having manufacturing errors," *Journal of Sound and Vibration*, vol. 329, no. 4, pp. 371–393, 2010.

[48] Z. Daneshi-Far, H. Henao, and G. A. Capolino, "Planetary Gearbox Effects on Induction Machine in Wind Turbine: Modeling and Analysis," in *Proceedings - 2012 20th International Conference on Electrical Machines, ICEM 2012*, 2012, pp. 1790–1796.

[49] R. G. R. G. Budynas, J. K. Nisbett, and J. E. Shigley, *Shigley's Mechanical Engineering Design*, 9th, Ed. McGraw-Hill, 2011.

[50] B. Armstrong-Hélouvry, *Control of Machines with Friction*. Kluwer Academic Publishers, 1991. [Online]. Available: https://link.springer.com/content/pdf/10.1007{%}2F978-1-4615-3972-8.pdf

[51] E. Oberg, F. Jones, H. Horton, H. Ryffel, and C. McCauley, *Machinery's Handbook*, 30th ed., 2016.

[52] D. B. Young, *Development Geology Reference Manual*. American Association of Petroleum Geologists Special Volumes, 1992, vol. 95. [Online]. Available: http://archives.datapages.com/data/specpubs/methodo1/data/a095/a095/0001/0050/0076.htm

[53] F. Chaari, W. Baccar, M. S. Abbes, and M. Haddar, "Effect of spalling or tooth breakage on gearmesh stiffness and dynamic response of a one-stage spur gear transmission," *European Journal of Mechanics, A/Solids*, vol. 27, no. 4, pp. 691–705, 2008.

[54] R. Ma, Y. Chen, and Q. Cao, "Research on dynamics and fault mechanism of spur gear pair with spalling defect," *Journal of Sound and Vibration*, vol. 331, no. 9, pp. 2097–2109, apr 2012. [Online]. Available: https://www.sciencedirect.com/science/article/pii/S0022460X11009382

[55] M. H. Marzebali, S. H. Kia, H. Henao, G. A. Capolino, and J. Faiz, "Planetary Gearbox Torsional Vibration Effects on Wound-Rotor Induction Generator Electrical Signatures," in *IEEE Transactions on Industry Applications*, vol. 52, no. 6, 2016, pp. 4770–4780.

[56] M. Amarnath, C. Sujatha, and S. Swarnamani, "Experimental studies on the effects of reduction in gear tooth stiffness and lubricant film thickness in a spur geared system," *Tribology International*, vol. 42, no. 2, pp. 340–352, 2009.

[57] J. Kim, I. Yang, D. Kim, M. Hamadache, and D. Lee, "Bearing fault effect on induction motor stator current modeling based on torque variations," *2012 12th International Conference on Control, Automation and Systems, ICCAS 2012*, pp. 814–818, 2012. [Online]. Available: http://www.scopus.com/inward/record.url?eid=2-s2.0-84872506518{&}partnerID=40{&}md5=de655b4b426f3a1582ced80f45345143

[58] Kugellager-Express, "Deep Groove Ball Bearing." [Online]. Available: https://www.kugellager-express.de/deep-groove-ball-bearing-6411-open-55x140x33-mm

[59] C. P. Mbo'O and K. Hameyer, "Modeling of a permanent-magnet excited synchronous machine with bearing damage," in *IECON Proceedings (Industrial Electronics Conference)*, 2014, pp. 3855–3860.

[60] T. A. Harris and M. N. Kotzalas, *Rolling Bearing Analysis*, 5th ed. CRC/Taylor & Francis, 2007.

[61] P. Večeř, M. Kreidl, and R. Šmíd, "Condition Indicators for Gearbox Condition Monitoring Systems," *Acta Polytechnica*, vol. 45, no. 6, pp. 35–43, 2005.

[62] J. W. Cooley and J. W. Tukey, "An Algorithm for the Machine Calculation of Complex Fourier Series," *Mathematics of Computation*, vol. 19, no. 90, p. 297, apr 1965. [Online]. Available: https://www.jstor.org/stable/2003354?origin=crossref

BIBLIOGRAPHY

Appendix A

Simscape Code

Listing A.1: Custom permanent magnet synchronous motor Simscape block.

```
component pmsm_custom

    nodes
        N = pe.electrical.three_phase.electrical;               % ~:left
        R = foundation.mechanical.rotational.rotational;        % R:right
        C = foundation.mechanical.rotational.rotational;        % C:right
    end

    parameters
        pole_pairs = {0, '1'};      % Number of pole pairs
        pm_flux    = {0, 'Wb'};     % Permanent magnet flux linkage
        Ld         = {0, 'H'};      % Stator d-axis inductance
        Lq         = {0, 'H'};      % Stator q-axis inductance
        Rs         = {0, 'Ohm'};    % Stator resistance
        N_ball     = {0, '1'};      % Number of balls/rollers
        d_inner    = {0, 'mm'};     % Inner race diameter
        d_outer    = {0, 'mm'};     % Outer race diameter
        D_ball     = {0, 'mm'};     % Ball diameter
        D_cage     = {0, 'mm'};     % Cage diameter
        r_a        = {0,  'mm'};    % Raceway groove radius
        beta       = {0, 'deg'};    % Contact angle
        alpha_m    = {0, '1'};      % Damage weighting related to load torque
        d_fault    = {0, 'mm'};     % Damage width
        J          = {0, 'kg*m^2'}; % Motor inertia
    end

    parameters (Access=protected)
        shift_3ph            = { [0, -2*pi/3, 2*pi/3], 'rad' }; % Phase shift
    end

    parameters(Access=private)
        s = D_ball/d_inner;
        N_outer = N_ball/2*(1-D_ball/D_cage*cos(beta)); % Number of times the ball crosses over the damaged bearing point inside a
                motor revolution
    end
```

```
    variables
        % Mechanical
        angular_position_diff = { 0, 'rad' };          % Rotor angle w.r.t. synchronous reference frame

        % Stator currents
        id                    = { 0, 'A' };            % d-axis current
        iq                    = { 0, 'A' };            % q-axis current
    end

    variables (Access=protected)
        torque                = { 0, 'N*m' };          % Mechanical torque
        I                     = { [0 0 0], 'A' };      % Stator currents
    end

    branches
        I          : N.I -> *;
        torque     : R.t -> C.t;
    end

    equations
        let
            angular_velocity = R.w - C.w;
            theta = pole_pairs*(angular_position_diff + wNominal*time);

            % dq0 transform
            abc2dq = 2/3*[cos(theta + shift_3ph);...
                        -sin(theta + shift_3ph)];

            % Va,Vb,Vc -> Vd,Vq
            vdq = abc2dq*N.V'
            vd = vdq(1);
            vq = vdq(2);

            % Flux linkages
            psi_d = id*Ld + pm_flux;
            psi_q = iq*Lq;

            % Electromagnetic torque equation
            t_em = -3/2*pole_pairs*(iq*psi_d - id*psi_q);

            % Bearing fault equations
            w_c = if angular_velocity > 0, 1/(2*(1+s))*R.w else 1e-10*{1, 'rad/s'} end;
            T = if angular_velocity > 0, 1/R.w else 1/w_c end;
            T_rect = T/N_outer;
            v_T = w_c*r_a;
            delta_dist = d_fault/v_T;
            A_dist = alpha_m*t_em;
            t_fault = bearing_fault(time,delta_dist,T_rect,A_dist);
        in
            % Electrical to mechanical rotation
            angular_velocity == wNominal + angular_position_diff.der;

            % Electrical equations
            vd == id*Rs + id.der*Ld - pole_pairs*angular_velocity*psi_q;
            vq == iq*Rs + iq.der*Lq + pole_pairs*angular_velocity*psi_d;
            [ id; iq ] == abc2dq*I';
            I(1)+I(2)+I(3) == 0;

            % Total torque
            torque == t_em + t_fault;
        end
    end
end
```

Listing A.2: Bearing fault Fourier series Simscape function. As each Fourier series component had to be explicitly written in the Simscape language, only an excerpt is provided. In total 60 Fourier series components were included in the function.

```
function t_dist = bearing_fault(t,delta_dist,T_rect,A_dist)
definitions

    a_f =  (2/(1*pi))*sin(value(delta_dist, 's')/value(T_rect, 's')*1*pi)*cos(1/T_rect*1*(t))+...
           (2/(2*pi))*sin(value(delta_dist, 's')/value(T_rect, 's')*2*pi)*cos(1/T_rect*2*(t))+...
           (2/(3*pi))*sin(value(delta_dist, 's')/value(T_rect, 's')*3*pi)*cos(1/T_rect*3*(t))+...
           (2/(4*pi))*sin(value(delta_dist, 's')/value(T_rect, 's')*4*pi)*cos(1/T_rect*4*(t))+...
           (2/(5*pi))*sin(value(delta_dist, 's')/value(T_rect, 's')*5*pi)*cos(1/T_rect*5*(t))+...
                                    .
                                    .
                                    .
           (2/(60*pi))*sin(value(delta_dist, 's')/value(T_rect, 's')*60*pi)*cos(1/T_rect*60*(t));

        t_dist = A_dist*ceil(a_f);
    end
end
```

Listing A.3: Custom planetary gear Simscape block.

```
component pg_custom

    nodes
        S = foundation.mechanical.rotational.rotational; % S:left
        C = foundation.mechanical.rotational.rotational; % C:right
    end

    parameters
        N_s        = {1,  '1'};          % Number of sun gear teeth
        N_p        = {1,  '1'};          % Number of planet gear teeth
        N_r        = {1,  '1'};          % Number of ring gear teeth
        p          = {1,  '1'};          % Number of planet gears
        m_p        = {1,  'kg'};         % Planet gear mass
        J_p        = {1,  'kg*m^2'};     % Planet gear inertia
        J_s        = {1,  'kg*m^2'};     % Sun gear inertia
        J_c        = {1,  'kg*m^2'};     % Carrier inertia
        r_bs       = {1,  'm'};          % Sun gear base radius
        r_bp       = {1, 'm'};           % Planet gear base radius
        r_bc       = {1,  'm'};          % Carrier base radius
        r_br       = {1,  'm'};          % Ring gear base radius
        k_max      = {1,  'N/m'};        % Maximum gear mesh stiffness
        k_min      = {1,  'N/m'};        % Minimum gear mesh stiffness
        k_loss_sp  = {1,  'N/m'};        % Sun-planet mesh stiffness loss due to a gear fault
        k_loss_rp  = {1,  'N/m'};        % Ring-planet mesh stiffness loss due to a gear fault
        z          = {1,  '1'};          % Damping rate
        w_ss       = {1,  'rad/s'};      % Steady state sun gear velocity
    end

    parameters(Access=private)
        k_mean = (k_max-k_min)/2 + k_min;
        c_sp = 2*z*sqrt(k_mean*J_s*J_p/(r_bs^2*J_p+r_bp^2*J_s));
        c_rp = 2*z*sqrt(k_mean*J_p/(r_bp^2));
    end
```

```
    variables
        T_s    = { 0, 'N*m' };   % Sun gear, incoming torque
        T_c    = { 0, 'N*m' };   % Carrier, outgoing torque
        q_c    = { 0, 'rad' };   % Carrier angular displacement
        q_s    = { 0, 'rad' };   % Sun gear angular displacement
        q_p1   = { 0, 'rad' };   % 1st planet gear angular displacement
        q_p2   = { 0, 'rad' };   % 2nd planet gear angular displacement
        q_p3   = { 0, 'rad' };   % 3rd planet gear angular displacement
    end

    branches
        T_s : S.t -> *;
        T_c : O.t -> *;
    end

    equations
        let
            k_sp1 = meshstiffness(k_max,k_min,k_loss_sp,w_ss,time,N_s,1,p);
            k_sp2 = meshstiffness(k_max,k_min,k_loss_sp,w_ss,time,N_s,2,p);
            k_sp3 = meshstiffness(k_max,k_min,k_loss_sp,w_ss,time,N_s,3,p);
            k_rp1 = meshstiffness(k_max,k_min,k_loss_rp,w_ss,time,N_s,1,p);
            k_rp2 = meshstiffness(k_max,k_min,k_loss_rp,w_ss,time,N_s,1,p);
            k_rp3 = meshstiffness(k_max,k_min,k_loss_rp,w_ss,time,N_s,1,p);
        in
            S.w == q_s.der;
            O.w == q_c.der;

            % Sun gear
            J_s*S.w.der+...
                r_bs*(c_sp*((r_bs*S.w-r_bc*O.w+r_bp*q_p1.der)+(r_bs*S.w-r_bc*O.w+r_bp*q_p2.der)+(r_bs*S.w-r_bc*O.w+r_bp*q_p3.der)))+...
                r_bs*((r_bs*q_s-r_bc*q_c)*(k_sp1+k_sp2+k_sp3)+r_bp*(k_sp1*q_p1+k_sp2*q_p2+k_sp3*q_p3)) == T_s;

            % Carrier
            (J_c+m_p*r_bc^2)*O.w.der-...
                r_bc*(c_sp*((r_bs*S.w-r_bc*O.w+r_bp*q_p1.der)+(r_bs*S.w-r_bc*O.w+r_bp*q_p2.der)+(r_bs*S.w-r_bc*O.w+r_bp*q_p3.der)))-...
                r_bc*(c_rp*((-r_bc*O.w-r_bp*q_p1.der)+(-r_bc*O.w-r_bp*q_p2.der)+(-r_bc*O.w-r_bp*q_p3.der)))-...
                r_bc*(k_sp1*(r_bs*q_s-r_bc*q_c+r_bp*q_p1)+k_sp2*(r_bs*q_s-r_bc*q_c+r_bp*q_p2)+k_sp3*(r_bs*q_s-r_bc*q_c+r_bp*q_p3))-...
                r_bc*(k_rp1*(-r_bc*q_c-r_bp*q_p1)+k_rp2*(-r_bc*q_c-r_bp*q_p2)+k_rp3*(-r_bc*q_c-r_bp*q_p3)) == T_c;

            % Planet 1
            J_p*q_p1.der.der+...
                r_bp*((c_sp*(r_bs*S.w-r_bc*O.w+r_bp*q_p1.der))-(c_rp*(-r_bc*O.w-r_bp*q_p1.der)))+...
                r_bp*((k_sp1*(r_bs*q_s-r_bc*q_c+r_bp*q_p1))-(k_rp1*(-r_bc*q_c-r_bp*q_p1))) == 0;

            % Planet 2
            J_p*q_p2.der.der+...
                r_bp*((c_sp*(r_bs*S.w-r_bc*O.w+r_bp*q_p2.der))-(c_rp*(-r_bc*O.w-r_bp*q_p2.der)))+...
                r_bp*((k_sp2*(r_bs*q_s-r_bc*q_c+r_bp*q_p2))-(k_rp2*(-r_bc*q_c-r_bp*q_p2))) == 0;

            % Planet 3
            J_p*q_p3.der.der+...
                r_bp*((c_sp*(r_bs*S.w-r_bc*O.w+r_bp*q_p3.der))-(c_rp*(-r_bc*O.w-r_bp*q_p3.der)))+...
                r_bp*((k_sp3*(r_bs*q_s-r_bc*q_c+r_bp*q_p3))-(k_rp3*(-r_bc*q_c-r_bp*q_p3))) == 0;
        end
    end
end
```

Listing A.4: Planetary gear time-varying mesh stiffness Fourier series Simscape function. As each Fourier series component had to be explicitly written in the Simscape language, only an excerpt is provided. In total 60 Fourier series components were included in the function.

```
function k_m = meshstiffness(k_max,k_min,k_loss,w,t,N_s,x,p)
definitions

     a_h =  (2/(1*pi))*sin(1*pi*1/2)*cos(1*(w*N_s)*(t))+...
            (2/(2*pi))*sin(2*pi*1/2)*cos(2*(w*N_s)*(t))+...
            (2/(3*pi))*sin(3*pi*1/2)*cos(3*(w*N_s)*(t))+...
            (2/(4*pi))*sin(4*pi*1/2)*cos(4*(w*N_s)*(t))+...
            (2/(5*pi))*sin(5*pi*1/2)*cos(5*(w*N_s)*(t))+...
                                    .
                                    .
                                    .
            (2/(60*pi))*sin(60*pi*1/2)*cos(60*(w*N_s)*(t));

     a_f =  (2/(1*pi))*sin((1/N_s)*1*pi)*cos(1*(w)*t-2*pi*1*(x/p+1/(p*N_s)))+...
            (2/(2*pi))*sin((1/N_s)*2*pi)*cos(2*(w)*t-2*pi*2*(x/p+1/(p*N_s)))+...
            (2/(3*pi))*sin((1/N_s)*3*pi)*cos(3*(w)*t-2*pi*3*(x/p+1/(p*N_s)))+...
            (2/(4*pi))*sin((1/N_s)*4*pi)*cos(4*(w)*t-2*pi*4*(x/p+1/(p*N_s)))+...
            (2/(5*pi))*sin((1/N_s)*5*pi)*cos(5*(w)*t-2*pi*5*(x/p+1/(p*N_s)))+...
                                    .
                                    .
                                    .
            (2/(60*pi))*sin((1/N_s)*60*pi)*cos(60*(w)*t-2*pi*60*(x/p+1/(p*N_s)));

      k_m = (k_max-k_min)*(a_h) - k_loss*(a_f) + (k_max-k_min)*2;
   end
end
```

Appendix B

Simulink Diagrams

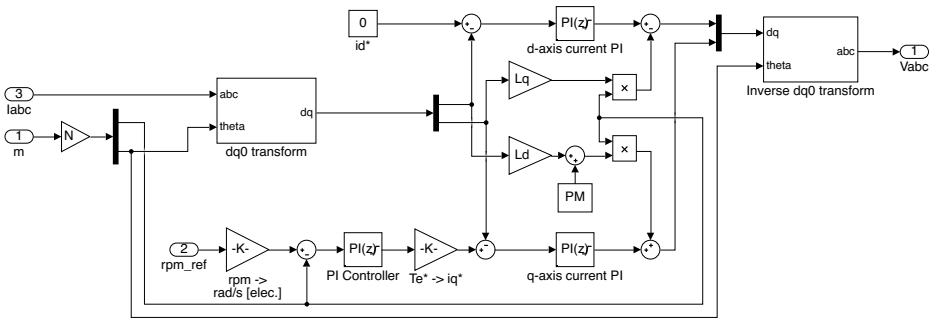

Figure B.1: PMSM controller Simulink diagram.

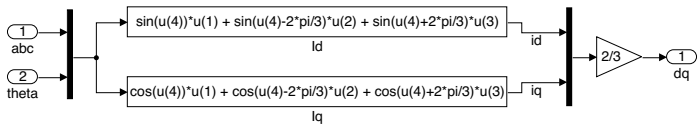

Figure B.2: $dq0$-transform Simulink diagram.

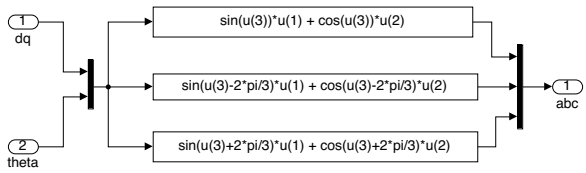

Figure B.3: Inverse $dq0$-transform Simulink diagram.

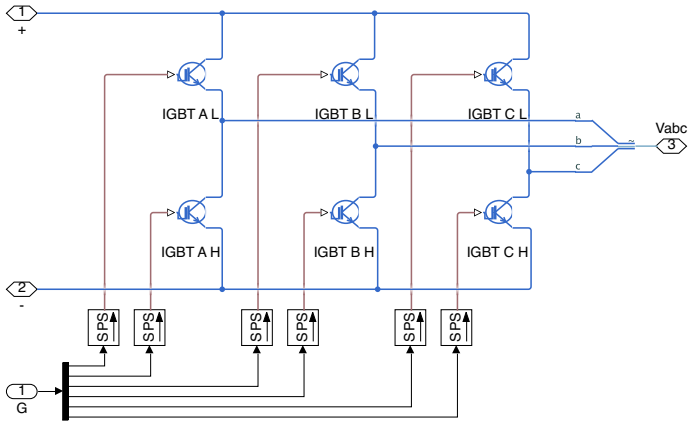

Figure B.4: Inverter Simulink diagram.

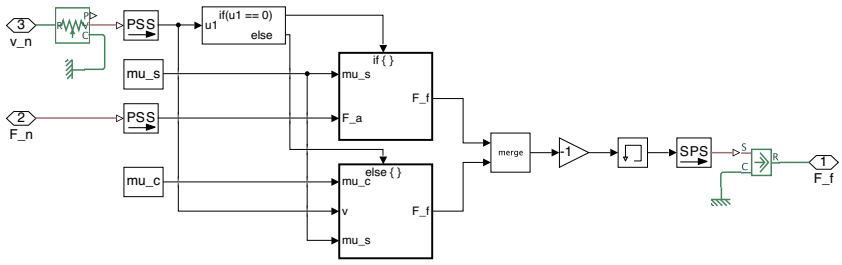

Figure B.5: Friction model Simulink diagram.

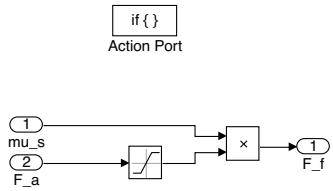

Figure B.6: Friction model for $v = 0$ Simulink diagram.

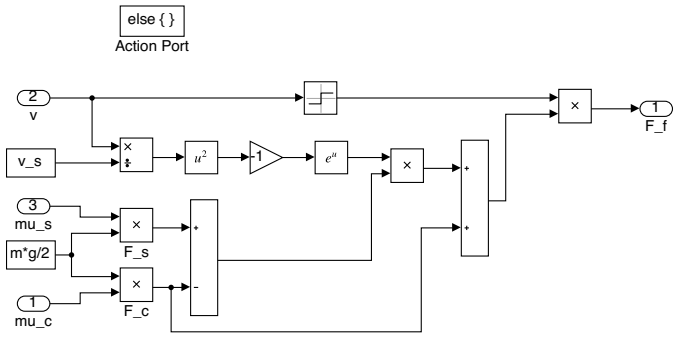

Figure B.7: Friction model for $v > 0$ Simulink diagram.

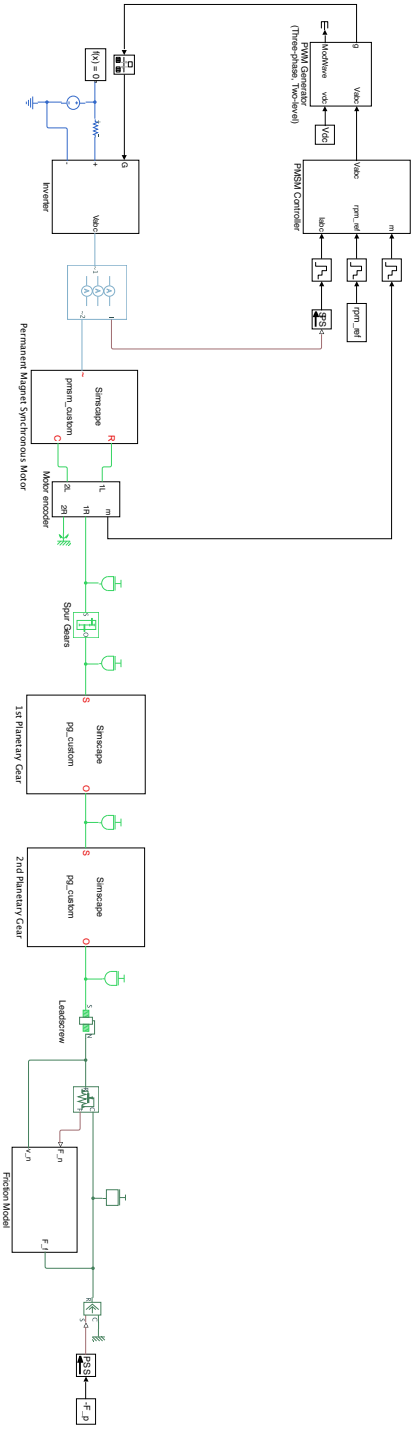

Figure B.8: Electro-mechanical shear ram actuator model Simulink diagram.

Appendix C

Matlab Code

Listing C.1: Matlab code used for FFT plot.

```
load('data.mat');
time = get(data,'Time');
x = get(data,'Data');

time = time(600000:end);
x = x(600000:end);

L = size(x,1);                          % Vector length
Ts = mean(diff(time));                  % Sampling interval
Fs = 1/Ts;                              % Sampling frequency
Fn = Fs/2;                              % Nyquist frequency
t = (0:L-1)/Fs;                         % Total time

Y = fft(x);                             % Fast Fourier Transform (FFT)
amp = abs(Y);                           % Amplitude of FFT
f = (0:L-1)*(Fs/L);                     % Frequency
x = x - mean(x);                        % Remove (constant) offset
Ys = fft(x)/L;                          % Scaled FFT
Fv = linspace(0, 1, fix(L/2)+1)*Fn;     % Frequency vector
Iv = 1:length(Fv);                      % Index vector

% Plot
figure(1)
plot(Fv, 2*abs(Ys(Iv)))
xlabel('Frequency (Hz)')
ylabel('Y(f)')
grid
```